

1 **Geophysical and geochemical multi-method investigations for reconstructing**
2 **subsurfaces, alluvial sedimentology, and structural geology (Tiber valley, Rome)**

3
4 Francesca Giustini^{1*}, Mauro Brilli¹, Giorgia Carlucci¹, Giancarlo Ciotoli^{1,2}, Iolanda Gaudiosi¹,
5 Marco Mancini¹, Maurizio Simionato¹

6
7 ¹ Istituto di Geologia Ambientale e Geoingegneria, CNR, Area della Ricerca di Roma1, Via Salaria
8 Km 29,300, 00015 Monterotondo Stazione, Roma, Italy.

9 ² Istituto Nazionale di Geofisica e Vulcanologia, Sezione Roma1, Via di Vigna Murata 605, 00143,
10 Roma, Italy

11 * Corresponding author at: francesca.giustini@igag.cnr.it
12

13
14 **Abstract**

15 Geophysical and geochemical methods were applied to detect the subsurface setting of an Upper Pleistocene-Holocene
16 fluvial incised-valley where a travertine body intercalates between alluvial deposits of the Tiber river (central Italy), at
17 Prima Porta (close to Rome). This study allowed us to provide more information regarding the local stratigraphic
18 architecture and structural features, as a reference analogue to similar settings: i.e., hard (stiff) lithic travertines buried
19 below fine and loose alluvial plain covers.

20 Two Electrical Resistivity Tomography (ERT) profiles, interpreted and calibrated using previously collected litho-
21 stratigraphic data from a borehole, identified a massive body, with a relatively high resistivity that correlates with the
22 travertine deposit of Prima Porta. In addition to ERT, ambient noise measurements, processed with the HVSR technique
23 and 2D array, and seismic refraction tomography were carried out; HVSR data were highly consistent with ERT results
24 and allowed to discriminate between the travertine body and the silty-sand channels and overbank deposits, which were
25 attributed to the Tiber river's evolution during Upper Pleistocene-Holocene. Finally, the presence of cracks/fractures
26 could be inferred, as suggested by slight polarisation effects recorded in the HVSR results and soil-gas anomalies.

27
28 **Keywords:** buried travertine deposit, Electrical Resistivity Tomography, ambient noise measurement, soil-gas survey,
29 Tiber valley, Upper Pleistocene, Holocene.

30

31

32 1. INTRODUCTION

33 Geophysical methods, such as seismic methods, ground penetrating radar, and electrical resistivity tomography, are
34 widely used to detect the subsoil structures of recent alluvial plains, where the lack of adequate outcrops prevents a
35 detailed reconstruction of buried stratigraphic and morpho-structural elements (Bridge, 2003; Miall, 2014). Similarly, in
36 these settings (i.e., alluvial plains), geochemical investigations have been used to infer the presence of morpho-
37 structural discontinuities buried below the sediment cover (Klusman, 1993; Ciotoli et al., 2007).

38 Here, we propose an integrated geophysical-geochemical approach aimed at defining the main features of the shallow
39 subsoil of a portion of alluvial plain in the Tiber valley, central Italy, just north of Rome; this portion is considered as a
40 case study and possible methodological reference for similar settings.

41 The Tiber valley corresponds to a NNW–SSE trending extensional basin that has been developing since the early
42 Pliocene along the western flank of central Apennines (Funicello and Parotto, 1978; Malinverno and Ryan, 1986;
43 Barberi et al., 1994). Most of the basin-fill consists of fluvial and deltaic deposits; the most recent deposits, which
44 pertain to the valley’s actual alluvial depocenter, consist of gravels and sands or silty sands alternating with floodplain
45 muds. As a morpho-tectonic depression of extensional origin, the valley is bounded by dominant NNW-SSE trending
46 normal faults and subordinate transversal fault systems, which may represent important routes for ascending,
47 mineralised hot waters whose manifestations are visible in some places, especially along the borders (such as those
48 which emerge in our case study) but also towards the centre (Giustini et al., 2018); in general, the deposition of
49 continental carbonate bodies associated with these manifestations is always evident. In fact, especially along its western
50 boundary, several deposits of continental carbonates crop out and/or are locally buried under the prevailing siliciclastic
51 alluvial deposits of the Tiber river (Tentori et al., 2016; Giustini et al., 2018). The reconstruction of the sedimentary
52 sequence within the central portion of the valley is impossible unless drilled cores are investigated.

53 Recently, an Upper Pleistocene travertine body of about 4 m in thickness, intercalated between Holocene and upper
54 Pleistocene alluvial deposits, was identified in an 18 m deep borehole at Prima Porta, north west of Rome, and at a
55 distance of 400 m from the right bank of the Tiber river, (Giustini et al., 2020). The borehole, drilled for agricultural
56 water supply, revealed CO₂-dominated free gas emissions and the presence of mineralised, hypothermal waters that
57 were recorded a few metres below the field level.

58 To comprehend the alluvial sedimentary sequence and the travertine body in relation to the gas emissions, the
59 groundwater, and the local structural geology, a knowledge of the subterranean sedimentary setting is needed.

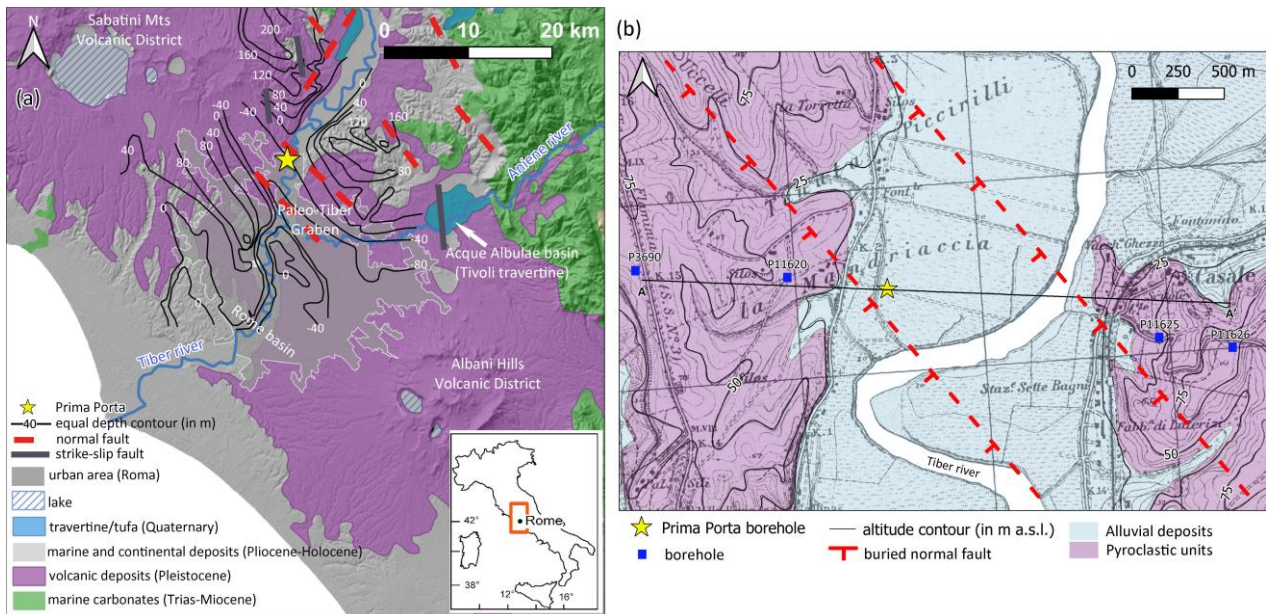
60 Geophysical methods may conveniently be used for this type of investigation. In the present paper, we investigated the
61 subterranean sediment sequence of Prima Porta using the Electrical Resistivity Tomography (ERT) which allows
62 remarkable penetration depths even if the presence of fluids can mask the geoelectrical contrasts between geological

63 formations (Loke and Barker, 1996; Loke and Dahlin, 2002). The ERT technique has been successfully applied in
64 several studies in which travertines were embedded within different sediments (Qarqori et al., 2012; De Filippis et al.,
65 2013; Pola et al., 2014; Huerta et al., 2016; Török et al., 2019). In the present paper, ERT was coupled with spectral
66 measurements of seismic ambient noise (Horizontal to Vertical Spectral Ratio - HVSr technique) (Nakamura, 1989;
67 Lunedei and Malischewsky, 2015; Sánchez-Sesma, 2017, and references therein). This technique was used to study
68 subsoil settings by means of determining the seismic velocity contrasts that locate interfaces between sedimentary
69 bodies with different mechanical characteristics. As an area characterised by rising mineralised waters and natural
70 gases, geochemical soil-gas prospection was also used to investigate the most likely routes of fluid flowing through the
71 strata up to the atmosphere in subterranean settings (Klusman, 1993; Ciotoli et al., 2007).
72 The aim of this study is to test a multimethod approach for reconstructing buried stratigraphic and structural features
73 and demonstrate their complementarity and ability to compensate the limits of each one.

74

75 **2. GEOLOGICAL FRAMEWORK**

76 The study area is located in the lower valley of the Tiber river, north of Rome and west of the central Apennines (Fig.
77 1a). The investigated Prima Porta site is located in the Tiber alluvial plain which crosses, along the NNE-SSW
78 direction, a hilly belt consisting of Pliocene-Quaternary sedimentary and pyroclastic deposits. In particular, the study
79 area lies in the inner convex bank of an eastward-directed meander of the Tiber (Fig. 1b).
80 Structurally, the valley corresponds to a morpho-tectonic depression of extensional origin, the Rome Basin, bounded by
81 dominant NNW-SSE trending normal faults and subordinate SW-NE directed transfer faults; short N-S trending dextral
82 strike slip faults are also found within the basin (Faccenna and Funicello, 1993).
83 Since the Early Pliocene, the extensional regime related to the opening of the Tyrrhenian Sea back arc basin has
84 controlled the growth and development of the Rome basin (Funicello and Parotto, 1978; Malinverno and Ryan, 1986;
85 Barberi et al., 1994). The pre-rift succession comprises Trias to Miocene calcareous, cherty, and siliciclastic pelagic
86 sequences, which were stacked to form the Apennine Chain fold-thrust belt during the Tortonian-Messinian (Patacca et
87 al., 1990; Cosentino et al., 2010). The Pliocene-Quaternary syn-rift successions consist of marine, transitional, and
88 continental sediments (up to 1 km in thickness) covering the pre-rift limestones and turbidites with an angular
89 unconformity.



90

91 **Fig. 1.** a) Geological map of the Tiber valley showing the location of the Prima Porta site: geology from SGI-ISPRA,
 92 faults from Faccenna (1994), equal depth contour from Funicello et al. (1992); b) Sketch map of the Prima Porta area:
 93 geology from the Geological Map of the Lazio Region, scale 1:25,000 and topography from 1:25,000 topographic maps
 94 of Italy from the Istituto Geografico Militare. The trace of the cross section A-A' (Fig. 2a), location of the boreholes
 95 (from Ventriglia, 2002; Di Bella et al., 2002), and buried inferred normal faults (from Funicello et al., 1992) are also
 96 drafted. Modified from Giustini et al. (2020).
 97

98 Since the late Early Pleistocene (~1.3 Ma), active uplift has affected the whole area, which has led to the emergence of
 99 the former sea floor. This phase was dominated by the fluvial sedimentation of the juvenile Tiber river ("Paleotiber" in
 100 Funicello et al., 1994; Mancini and Cavinato, 2005; Mancini et al., 2007) and by the deposition of eruptive products
 101 from the Sabatini Mts and Albani Hill volcanic districts (De Rita et al., 1993; Sottili et al., 2004; Funicello and
 102 Giordano, 2010). The ancient Tiber river incised the Pliocene-Early Pleistocene marine clay and silt defining a NNW-
 103 SSE trending deep paleo-valley, filled with gravels, sands, and minor mud. These deposits rarely crop out since they are
 104 buried below younger pyroclastic successions (ignimbrites, phreato-magmatic ashes, pumice, and ash falls), dated at
 105 approximately 600-280 ka (Barberi et al., 1994), and locally by Upper Pleistocene-Holocene fluvial deposits.
 106 The Prima Porta site is, in fact, located on the west side of the recent Tiber's alluvial plain that, in this area, is ~2 km
 107 wide and has elevations ranging from 19 to 22 m above sea level (Fig. 1b). NNW-SSE trending normal faults, inferred
 108 from Funicello et al. (1992), bound the ancient paleo-valley to the north-east and are those and are related to the
 109 development of the Paleotiber graben, buried by younger pyroclastic successions and fluvial deposits.
 110 The alluvial plain corresponds to the top of the fluvial incised-valley fill of the Upper Pleistocene-Holocene Tiber
 111 Depositional Sequence or TDS (Milli et al., 2016) (Fig. 2a). The last cycle of sea level changes (from MIS5d to MIS1;
 112 116-0 ka) controlled the valley fill, which comprises the complex stack of deposits belonging to the lowstand to
 113 transgressive and highstand systems tracts, totalling a thickness of 60 m.

114 The oldest TDS deposits are attributed to the early lowstand phase (116-26 ka) and define rare depositional terraces
115 perched on the incised-valley slopes and buried below more recent transgressive sediments. These terraces record short-
116 lived phases of sedimentation which occurred during the long phase of the lowering of base level.

117 Younger basal gravels, organised into amalgamated channel bodies in the deepest portion of the incised valley, and
118 overlaying channel sand and floodplain muds, are respectively ascribed to the late lowstand-early transgressive (26-14
119 ka) and late transgressive-highstand (14-0 ka) phases (Milli et al., 2016). In particular, the sands define channel-fill
120 bodies with different stacking patterns for the transgressive and the highstand systems tracts of TDS (Milli et al., 2016),
121 also related to the laterally confining floodplain fines: from relatively narrow and vertically accreted channel bodies of
122 the transgressive systems tract, with high rates of accommodation, to wider and laterally amalgamated channel bodies
123 of the highstand systems tract, with decreasing rates of accommodation and increasing channel clustering (see also
124 Schumm, 1993).

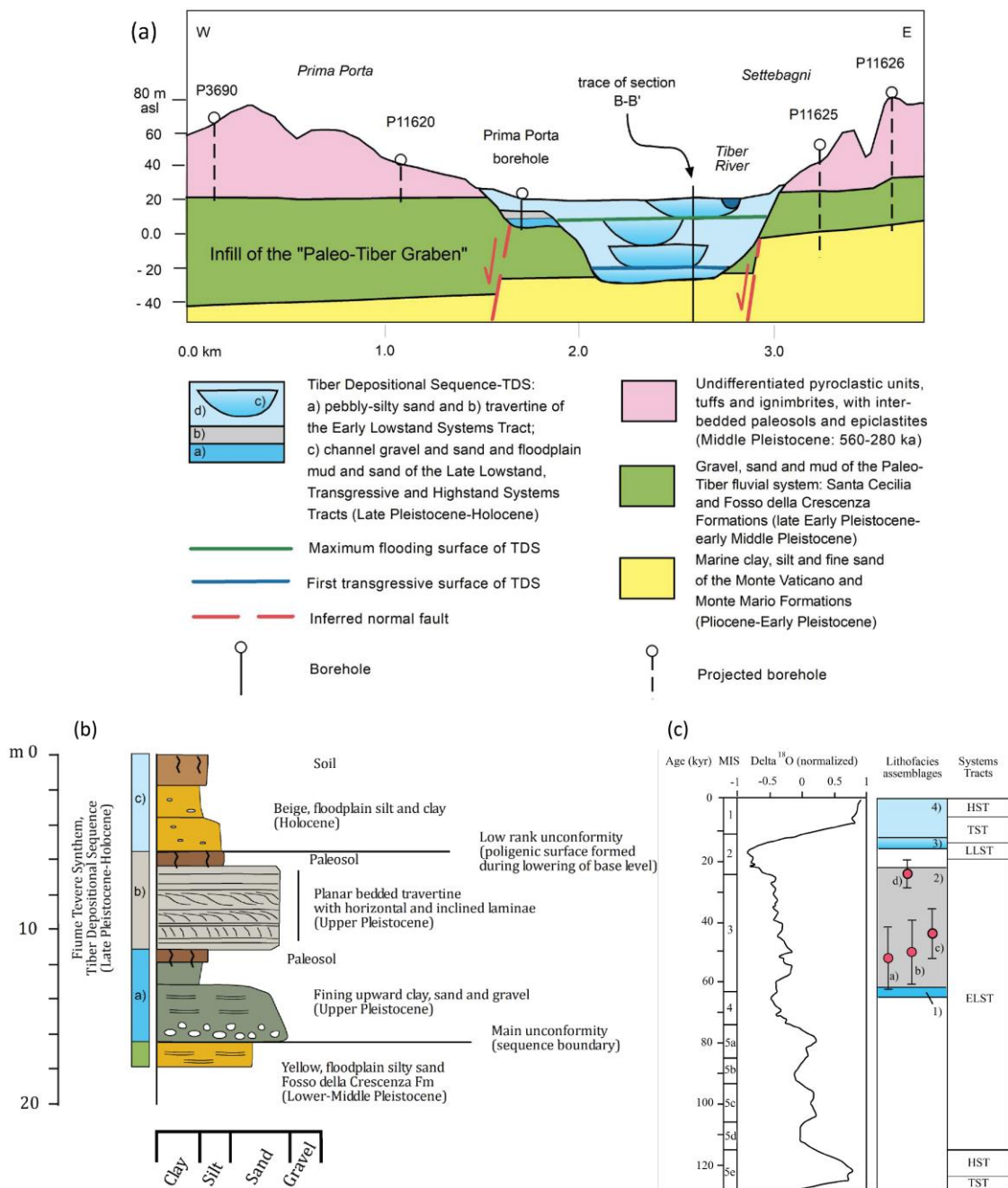
125 The stratigraphy of the 18 m-long core recovered at Prima Porta (Fig. 2b) corresponds to one of the detached
126 depositional terraces and overlying transgressive sediments (Giustini et al., 2020): above the basal layer, which consists
127 of 1.5 m thick yellow-beige massive silty sands, attributed to the Paleotiber unit (i.e., Fosso della Crescenza and Santa
128 Cecilia Formations, in Funicello and Giordano, 2008), a 11 m thick body represents the buried terrace; this is part of
129 the *Fiume Tevere* Synthem or TDS (according to Funicello and Giordano, 2008, or Milli et al., 2016, respectively), and
130 consists of a 5.5 m thick succession of grey, massive pebbly-silty sand and clay with sparse carbonate encrustations (unit
131 a), ~4 m of travertine at Prima Porta (unit b), and ~1 m of massive dark brown/red clayey paleosols (Fig. 2b). The
132 travertine was dated between 53.5 ± 10 ka to 24.2 ± 4.7 ka by U/Th method (Giustini et al., 2020) and can be correlated
133 to the MIS 3. The remaining upper sequence consists of beige massive silt and clay that record the recent phases (age
134 ≤ 6.0 ka, middle-late Holocene) of river flooding (unit c).

135

136 **2.1. The travertine of Prima Porta**

137 The travertine of Prima Porta macroscopically consists of a hard and quite dense crystalline material, which appears to
138 be structureless or with horizontally bedded and inclined layers which are a few centimetres to decimetres thick. These
139 features, as well as their microfacies associations (i.e., micrite crusts and rafts, both intercalated within and between the
140 shrubs), suggest that the deposition of this travertine was associated with low-to-moderate energy environments, such as
141 gently-dipping, shallow pools of low-angle terraced slopes (Giustini et al., 2020). Currently, the travertine of Prima
142 Porta is associated with hypothermal, saline water and deeply derived CO₂ gas emissions, whose ascent through the
143 rock units is probably connected with a crustal structural lineament (Giustini et al., 2018). Diagenetic alteration appears
144 to be limited, as inferred from macroscopic and petrographic observations (Giustini et al., 2020). The travertine was

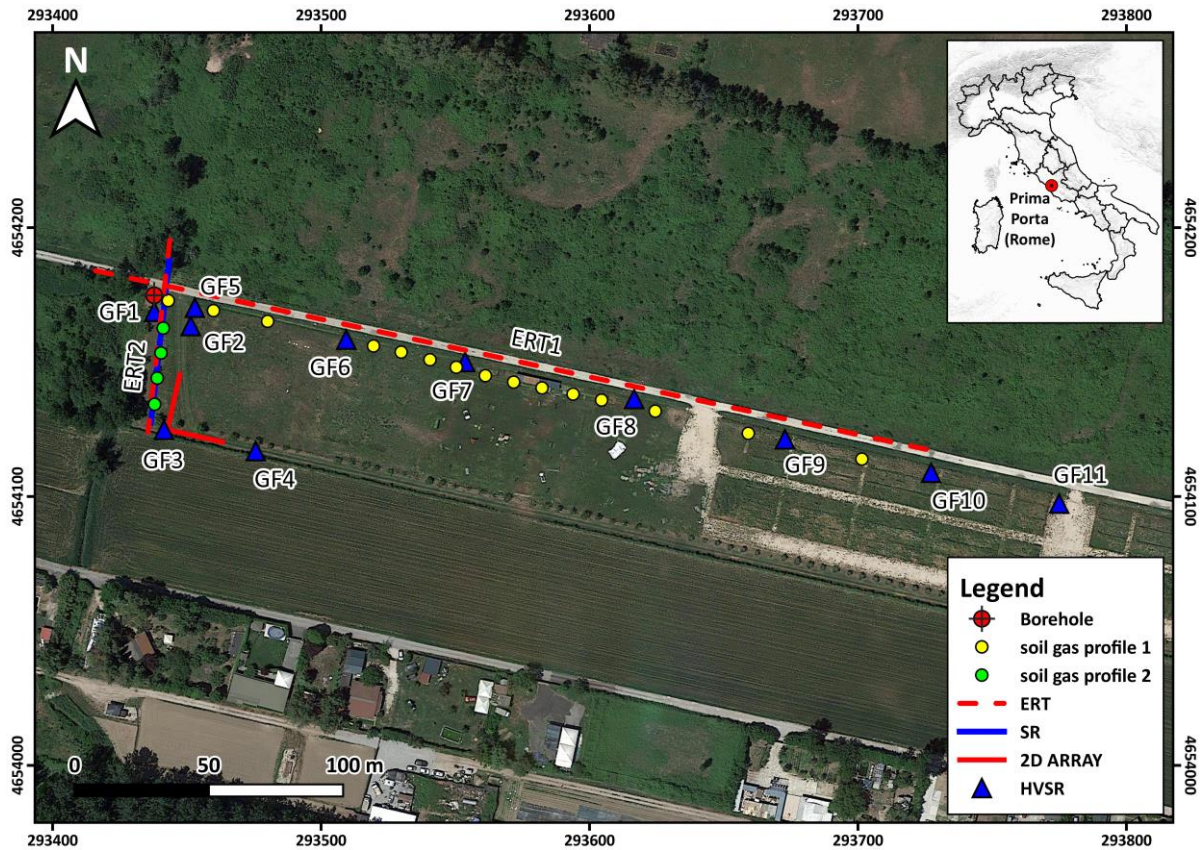
145 dated between 53.5 ± 10 ka to 24.2 ± 4.7 ka by U/Th method (Giustini et al., 2020), its deposition started approximately
 146 coevally with the wettest climatic conditions occurring during MIS3 (Fig. 2c), whereas the end of the deposition period
 147 coincides with the cold and arid phase of the last glacial maximum (Giustini et al., 2020).
 148



149
 150 **Fig. 2.** a) Geological cross sections showing the stratigraphic architecture of the middle Tiber valley, based on the
 151 geological map of Funicello and Giordano (2008) and borehole data from Di Bella et al. (2002) and Ventriglia (2002);
 152 b) Schematic section of the drilled core; the travertine deposit is embedded within alluvial sediments of the Tiber river.
 153 Reproduced from Giustini et al. (2020); c) Chronostratigraphic scheme of the Prima Porta deposit; Prima Porta
 154 travertine ages (red circles) are from Giustini et al. (2020), lithofacies assemblages correspond to the schematic section
 155 in b), oxygen isotope curve is from Martinson et al. (1987), Systems Tracts of the Tiber depositional sequence are based
 156 on Milli et al. (2016) (HST: Highstand Systems Tract; TST: Transgressive Systems Tract; LLST: Late Lowstand
 157 Systems Tract; ELST: Early Lowstand Systems Tract).
 158

159 **3. METHODS**

160 Different methods were applied to study the subsurface setting of the study area, including: electrical (ERT), surface
161 waves based (HVSr and 2D arrays), shallow seismic refraction, and geochemical (CO₂ and ²²²Rn soil-gas survey)
162 methods. Each method was processed separately and then a joint interpretation was performed. The location of the
163 measurements is shown in Figure 3.
164



166 **Fig. 3.** Aerial view of the study area with the location of the Prima Porta borehole, HVSr, 2D array, Electrical
167 Resistivity Tomography (ERT), Seismic Refraction (SR) surveys, and soil-gas measurements.
168

169 **3.1. Electrical Resistivity Tomography (ERT) surveys**

170 ERT surveys were carried out to determine the specific electrical resistivity ρ of the ground and to obtain 2D images of
171 its distribution in vertical ground sections.

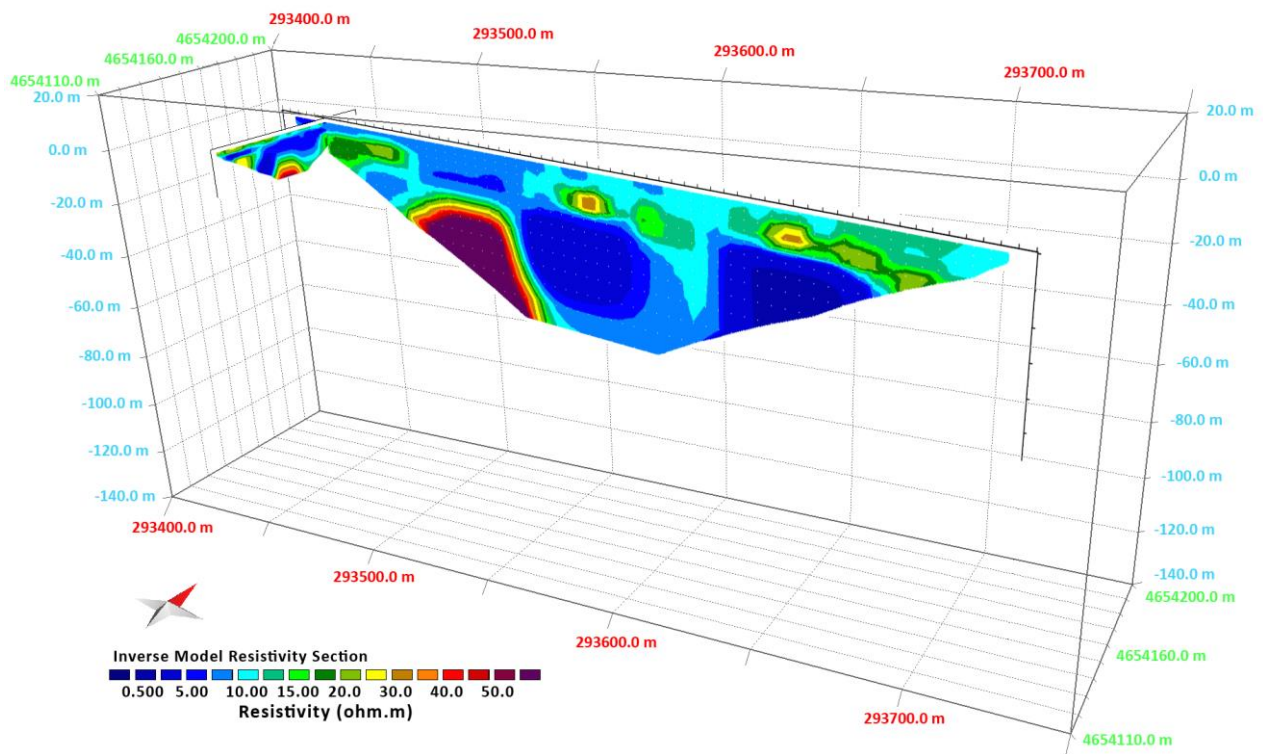
172 ERT consists of the application of a direct electrical current into the ground using a quadrupolar dispositive, the
173 acquisition of A/D converted data of voltages through a computer-controlled acquisition system, and the computation of
174 resistivity using Ohm laws. The quadrupole consists of two current electrodes, through which direct current is fed into
175 the ground, and two measuring electrodes, through which the voltage is measured. There are many different electrode
176 array configurations available, but all configurations are aimed at gathering data that can be used to estimate lateral and

177 vertical variations in ground resistivity values with different resolutions (Loke and Barker, 1996; Loke and Dahlin,
 178 2002).

179 Two ERT measurements were performed using a georesistivimeter 16SG model (Pasi, S.r.l.), equipped with 64
 180 electrodes with variable spacing using the Wenner-Schlumberger configuration. As conventionally reported in the
 181 literature, the depth of investigation is up to 1/5 or 1/6 of the total length of the electrical profile. Data were processed
 182 using the Res2dinv software from Geotomo Software. The 2D inversion is based on the robust constrained least-squares
 183 inversion implemented with a Gauss-Newton method.

184 The first measurement (ERT-1) was carried out in the W-E direction, using 64-electrodes with a 5 m electrode distance,
 185 which allows the 2D reconstruction of the resistivity trend in the subsoil up to a depth of about 50 m along a 315 m long
 186 profile. The ERT-1 profile crosses the Prima Porta borehole – whose stratigraphy is known (Fig. 2b) and which was
 187 used to calibrate the resistivity measurement – down to electrode n. 40. The second measurement (ERT-2) was
 188 performed with a N-S orientation; in this case, 48 electrodes were used with an electrode distance of 1.5 m and a total
 189 length of 70.5 m, reaching a depth of about 12 m. The two arrays intersect between the electrodes n. 40 of the W-E
 190 array and n. 7 of the N-S one, as shown in Figure 4.

191



192

193 **Fig. 4.** Inverted 2D resistivity models for the two perpendicular electrical resistivity tomographs. ERT-1 is oriented W-
 194 E; ERT-2 is oriented N-S. The models are displayed in perspective to visualise the 3D subsoil structure starting from
 195 the 2D cross-sectional images.

196

197 3.2. Ambient noise survey

198 A series of eleven ambient noise measurements, labelled from GF1 to GF11, was conducted along the two cross-
199 sections (Fig. 3). The equipment consisted of SS02 SARA velocimetric sensors with a cut-off frequency of 0.2 Hz,
200 connected to six-channel SL06 SARA data loggers. Data were recorded with a sample rate of 200 samples per second.
201 During installation, particular care was adopted to deploy sensors in order to guarantee an adequate coupling with the
202 ground and to avoid the positioning of the sensors directly over sources of disturbance. Shallow holes were realized to
203 emplace sensors and remove the possible disturbance of the grass.

204 Recordings of about one hour of noise were collected and the Horizontal to Vertical Spectral Ratio (HVSR) technique
205 was applied (Nakamura, 1989). This is a well-established approach: inferences for the subsurface seismic velocity
206 contrasts may be extrapolated from the retrieved peaks in the HVSR curves, considering for instance that shallower
207 interfaces produce higher peak frequencies. Each ambient vibration recording was divided into 50 s-long time windows
208 in the open-source software Geopsy (<http://www.geopsy.org/>) (Wathelet et al., 2020). We computed the amplitude
209 spectra for the vertical and horizontal components (north and east components). Spectra were smoothed using the
210 Konno and Omachi (1998) window with a b value of 40, while the horizontal spectra were computed from the north and
211 east components as: $\sqrt{(\text{north}^2 + \text{east}^2)}$ before computing the HVSR for each time window. Then, we computed the
212 average HVSR for each station.

213 In addition to the HVSR noise measurements at single stations, surface-wave methods were also applied, allowing the
214 acquisition of 2D array ambient vibrations data and one S-waves velocity profile. The latter was retrieved from a joint
215 inversion of Rayleigh dispersion curves with ellipticity. In more detail, 2D arrays are based on the acquisition of
216 ambient vibrations and the interpretation of the recordings obtained at synchronised seismic stations, or geophones
217 (seismic antenna) with the ground, according to different geometries. The geophones were arranged in a two-
218 dimensional L-shaped geometry with regular spacing (3 m on each side; see also Fig. S4b in Supplementary Materials).
219 Even if more regular and symmetrical shapes (circular or triangular shapes) are recommended in general, T or L shapes
220 are also possible (Foti et al., 2018). Thus, a L-shaped geometry can be a compromise among the number of sensors, the
221 operating time available and a desired highest resolution of the uppermost layer description. In this case, the choice of
222 limited inter-geophonic distance (3 m) and the consequentially maximum dimension of each branch lower than 36m
223 agreed with the necessity of exploring the presence of lateral heterogeneities and the first uppermost layers. The basic
224 scheme of the application of all surface-wave methods consists of three steps: i) measuring the wave trains of surface
225 waves by means of the arrays of seismic stations or geophones, suitably deployed on the surface; ii) estimating the
226 apparent dispersion curve of surface waves; and iii) solving the inverse problem to estimate the soil structure looking
227 for the best-fit between the experimental and theoretical dispersion curves. Joint inversions with the HVSR technique

228 related to Rayleigh wave ellipticity are generally performed to obtain more robust representative S-waves velocity
229 profiles. In this case, the dispersion curve was derived by applying two different methods: MSPAC (Modified SPatial
230 Auto-Correlation, Bettig et al., 2005) and the conventional beamforming f-k (Lacoss et al., 1969). The registrations of
231 the noise wave-field were performed for a minimum duration of 40 minutes with 24 vertical geophones (cut-off
232 frequency equal to 4.5 Hz). Geophones are equipped with spikes which serves as a screw to secure the coupling with
233 the ground. Also in this case, before emplacing geophones, the grass around each 1-component sensor was removed to
234 avoid any possible disturbance. Different codes were used: the Geopsy software (www.geopsy.org) (Wathelet et al.,
235 2020) was used to retrieve the dispersion curves for applying f-k and MSPAC analyses, while HV-inv (García-Jerez et
236 al., 2013, 2016; Piña-Flores et al., 2016; Sánchez-Sesma et al., 2011) was used for solving the inverse problem. Hv-inv
237 is based on the diffuse field assumption, therefore the resulting modelled ellipticity curve is comprehensive of both
238 Rayleigh and Love waves. Rayleigh wave ellipticity used for the joint inversion was defined directly from the HVSR
239 curve.

240

241 **3.3. Seismic refraction tomography survey**

242 Seismic refraction (SR) is generally applied to determine impedance contrast for engineering applications, to investigate
243 the depth to bedrock, as well as for groundwater exploration, crustal structure, and tectonics (Kilner et al., 2005;
244 Asokhai et al., 2008; Varughese et al., 2011; Chiemekwe and Aboh, 2012). The seismic refraction method is based on the
245 measurement of the travel time of seismic waves refracted at the interfaces between subsurface layers of different
246 velocity (Ayolabi et al., 2009). The seismic signal is introduced into the subsurface via a shot point using an elastic
247 wave generator. The energy generated either travels directly through the upper layer (direct arrivals) or down through
248 the various layers before returning to the surface (refracted arrivals). It is then detected at the surface by a series of
249 geophones (10 Hz), spaced at regular intervals. Both compressional waves (P-waves), which provide depth information
250 about the interfaces, and shear waves (S-waves), which provide additional data about the engineering properties of the
251 subsurface media, can be used in the seismic refraction method (Igboekwe and Ohaegbuchu, 2011; Gabr et al., 2012).
252 SR surveys use the process of critical refraction to infer interface depths and layer velocities. Based on the analysis and
253 inversion of the field data, seismic profiles are constructed to evaluate the thickness and type of materials of the
254 subsurface (Okiongbo et al., 2011). In this case study, the technique was usefully joined with the 2D array results: the
255 P-waves profile obtained was applied as a constraint for the dispersion curve inversion. In particular, the V_p model
256 obtained from the seismic refraction tomography survey was used as V_p profile max and min in the dispersion curve
257 joint inversion. The resulting Poisson's ratio is about 0.5 and is comparable with the value assumed of the uppermost
258 saturated deposits. The data are presented as cross-sectional plots representing the path, velocities, and depths of P-

259 waves to various interfaces. SR was performed along the aforementioned ERT-2, using a geophone inter-distance of 2.5
260 m for a total length of 57.5 m.

261

262 **3.4. Soil-gas survey**

263 Soil-gas measurements were performed along two profiles parallel to the ERT profiles, according to a sampling distance
264 ranging from 20 to 40 m. Nineteen soil-gas samples were collected using a well consolidated technique (Beaubien et al.,
265 2013; Ciotoli et al., 2007) consisting of pounding a 6.4 mm, thick-walled, stainless-steel probe into the soil at a depth of
266 about 0.6-0.8 m using a co-axial hammer; such a depth ensures the negligible influence of atmospheric air (Hinkle,
267 1994). A portable multi gas analyser (Draeger X-am 7000) directly connected to the probe was used to measure carbon
268 dioxide (CO₂) concentrations directly in the field. Soil-gas radon (²²²Rn) concentrations were measured with a portable
269 RAD7 alpha detector (Durrige Company Inc.), performing three/four measurements of radon and thoron activity each,
270 with a 5-minute integration time, and using a drying tube (filled with CaSO₄) to maintain the relative humidity below
271 10%.

272

273 **4. RESULTS**

274 **4.1. ERT profiles**

275 Two ERT profiles were performed along perpendicular directions. The first tomograph (ERT-1) was made in the W-E
276 direction, across the valley, and the second (ERT-2) in N-S direction, down the valley and located in the innermost
277 portion of the meander (Fig. 3). Resistivity values varied from 0.5 to 60 ohm×m; three zones could be distinguished on
278 the basis of these values (Fig. 4).

279 Zone 1, characterised by low resistivity (<15 ohm×m) is coloured in blue in Figure 4. In ERT-1, this zone appears quite
280 surficial between the metric coordinates of 80 and 150 m, and deeper than 20 m in the central-eastern part of the profile.
281 In ERT-2, the zone of low resistivity is located below 1.5 m and appears as a sub-horizontal layer (about 3 m thick) that
282 becomes increasingly deep between 40-50 m toward the south.

283 Zone 2 represents resistivities between 15 and 30 ohm×m, and is shown in green to yellow colours. In ERT-1, two
284 levels with resistivities between 15 and 30 ohm×m are recognised in the eastern and western parts of the tomograph,
285 disconnected by a low resistivity area in the centre. In ERT-2, Zone 2 is located just below surface and is about 1.5 m
286 thick. In addition, a level with resistivities between 15 and 30 ohm×m displays a concave-upward section wedging out
287 toward the central part of the profile, where the resistivity tends to increase up to 50 ohm×m. Finally, a lens of Zone 2 is
288 located in the eastern part of the profile, embedded within a low resistivity area.

289 Zone 3 is characterised by the highest resistivities ($>30 \text{ ohm}\times\text{m}$), shown in orange to purple colours. Zone 3 is well
290 represented in ERT-1 by a resistant block with a sharp lateral variation of resistivity in the central-western part of the
291 profile, whose top is at a depth of about 20 m.

292

293 **4.2. Ambient noise survey**

294 Results from noise measurements in terms of HVSR and single spectra are reported in Figures 5 and 6, respectively.

295 HVSR amplitude never overcomes the value of 2.5; therefore, a smooth change in impedance properties is expected.

296 Moreover, as seen in Figure 5, the mean HVSR at the GF1 to GF7 sites has amplitude values lower than 1, between

297 about 2 and 4 Hz; this may be associated with an inversion of S-wave velocity in the soil profile, i.e., the upper

298 sediments have a higher S-wave velocity than the underlying layers. Single spectra in Figure 6 would show a behaviour

299 traceable to stratigraphies with similar characteristics. In this case, the amplitude of the vertical component at the same

300 range of frequencies increases from the GF1 to GF5 and GF1 to GF7 sites and the vertical component has higher values

301 than those of the horizontal components. In these cases, as suggested from Castellaro and Mulargia (2009), local

302 minima of the vertical component associated with flat or local maxima in the horizontal ones have to be carefully

303 considered, since they may hide important HVSR peaks such as the one at 2.5 Hz.

304 Otherwise, both HVSR and single spectra at the GF8, GF9, GF10, and GF11 sites show the expected behaviour in the

305 case of a soil profile with S-wave velocities increasing with depth.

306 From the analyses of the single spectra, despite the high variability of the measured HVSR curves, it arises that the

307 predominant frequency f of the study area is 1.5 Hz in the range 1-10 Hz. A further peak occurs at frequencies lower

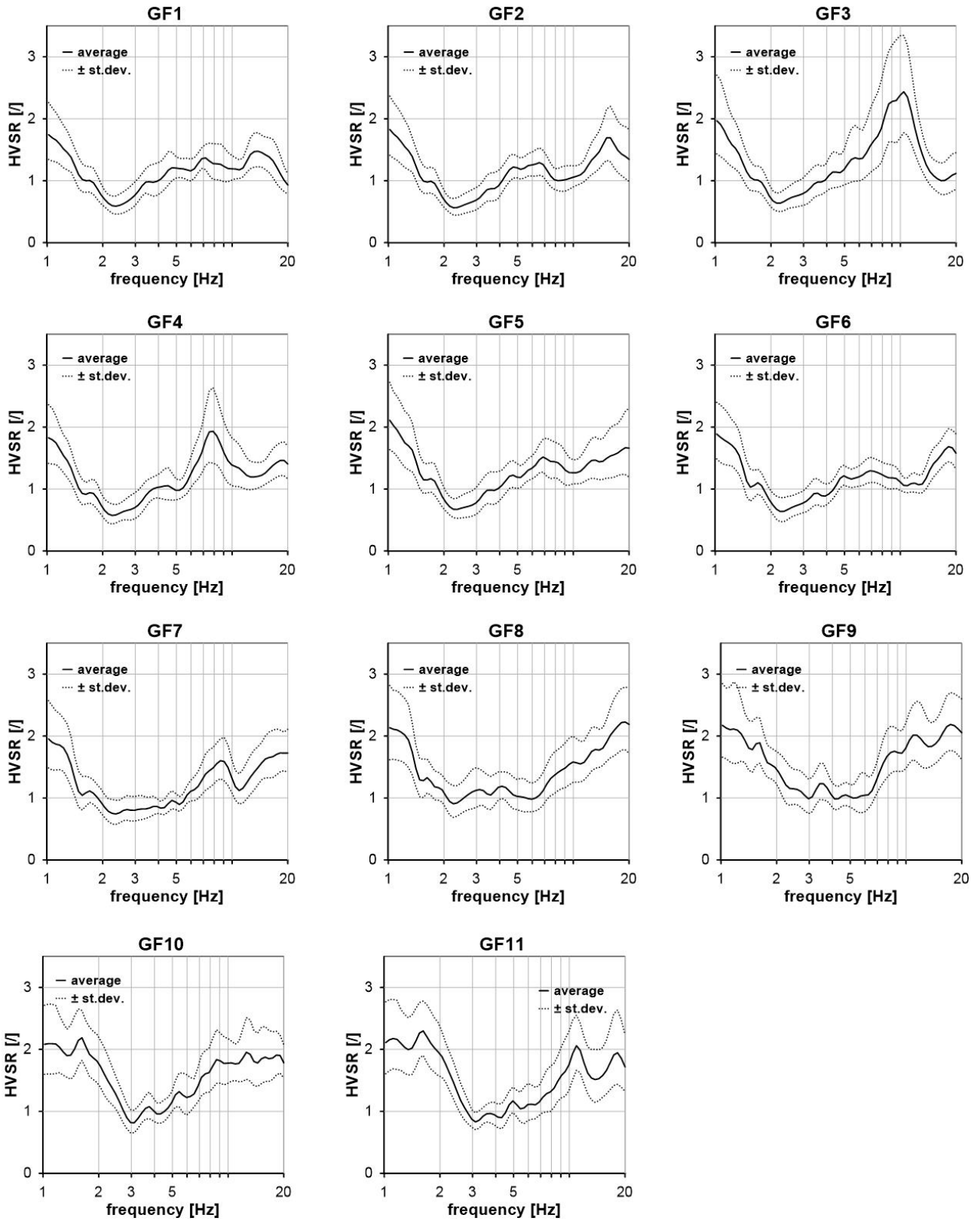
308 than 0.8 Hz. This is relative to the Tiber river valley resonance referring to the deepest bedrock interface (see Carlucci,

309 2017; Marcucci et al., 2019 and reference therein), and it was not considered because our study only focuses on the

310 characterisation of the first layers (up to 30-40 metres in depth). Another peculiar shape is recognisable at frequencies

311 greater than 5.

312



313

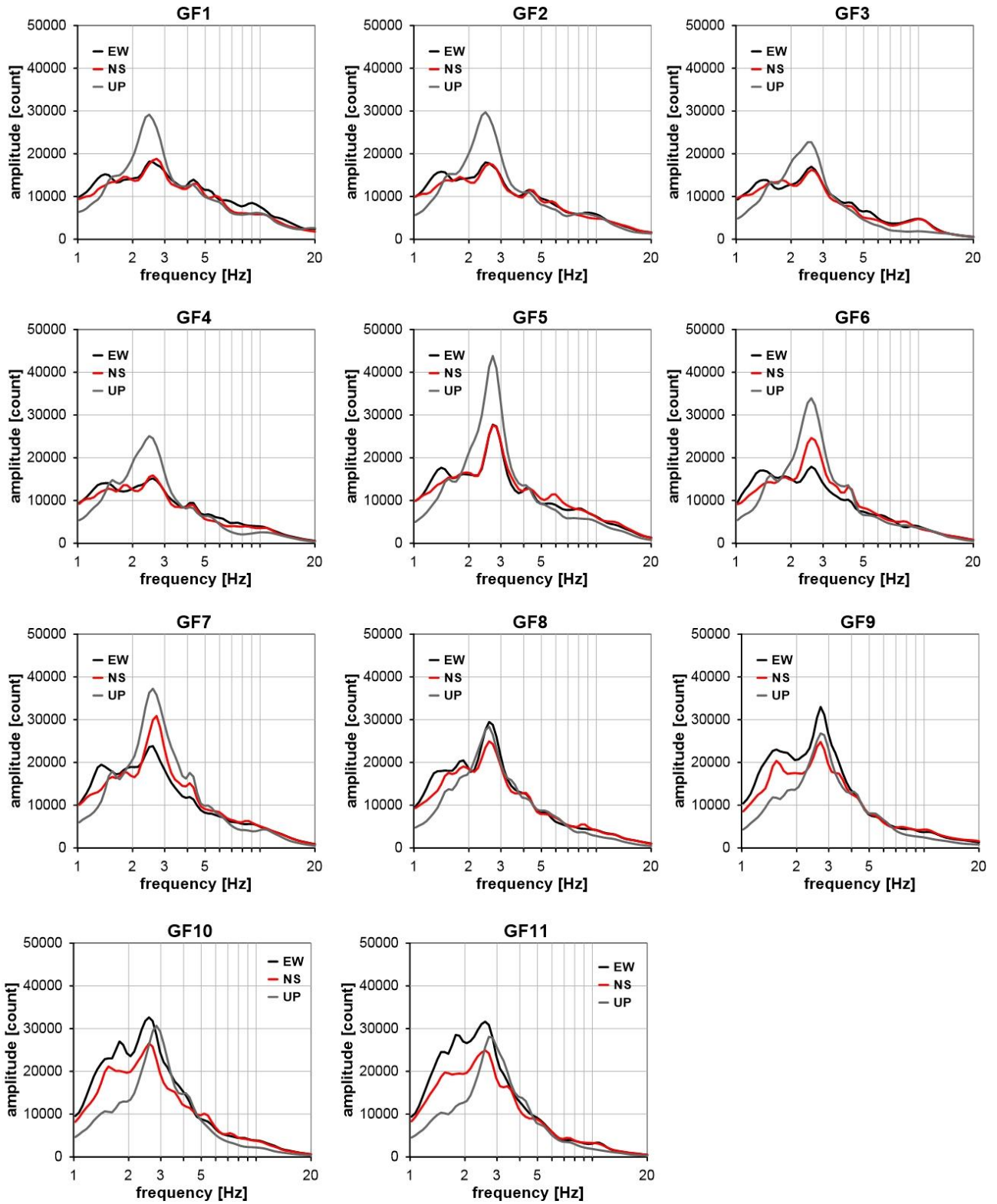
314

315

316

317

Fig. 5. Measured HVSR curves. Single plots refer to the band 1-20 Hz for the clarity. Curves plotted in the range 0.2-20 Hz may be found in the Supplementary Materials.

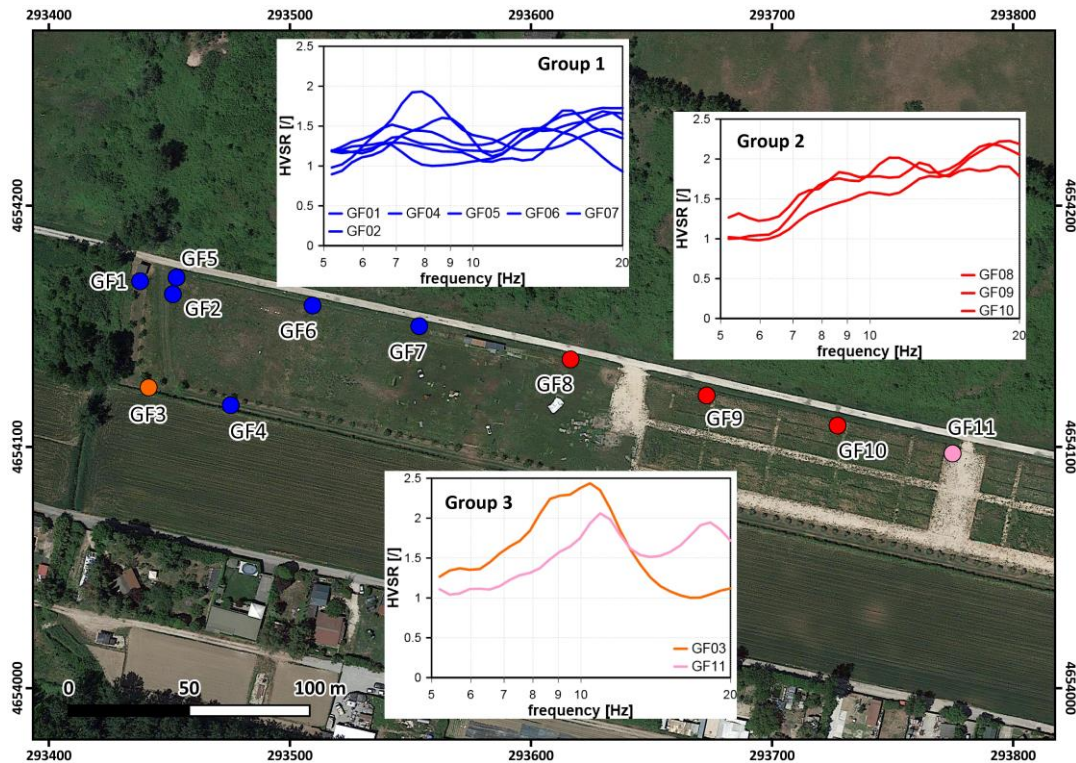


318

319 **Fig. 6.** Measured single spectra curves. Single plots refer to the band 1-20 Hz for the clarity. Curves plotted in the range
 320 0.2-20 Hz may be found in the Supplementary Materials.
 321

322 All these considerations led us to group the HVSR into three different clusters. The first cluster exhibits a bi-modal
 323 shape (in blue in Fig. 7); the second cluster shows a very broad band peak at a higher frequency which may be related to
 324 a 2D/3D subsurface model; and the third cluster shows a peak with very high amplitude values and one with HVSR

325 characterised by the clearest peaks (grouping GF3 and GF11). Both of them are quite different from those retrieved at
326 stations in their immediate vicinity, but further data would be necessary to retrieve insights about this behaviour.
327



328

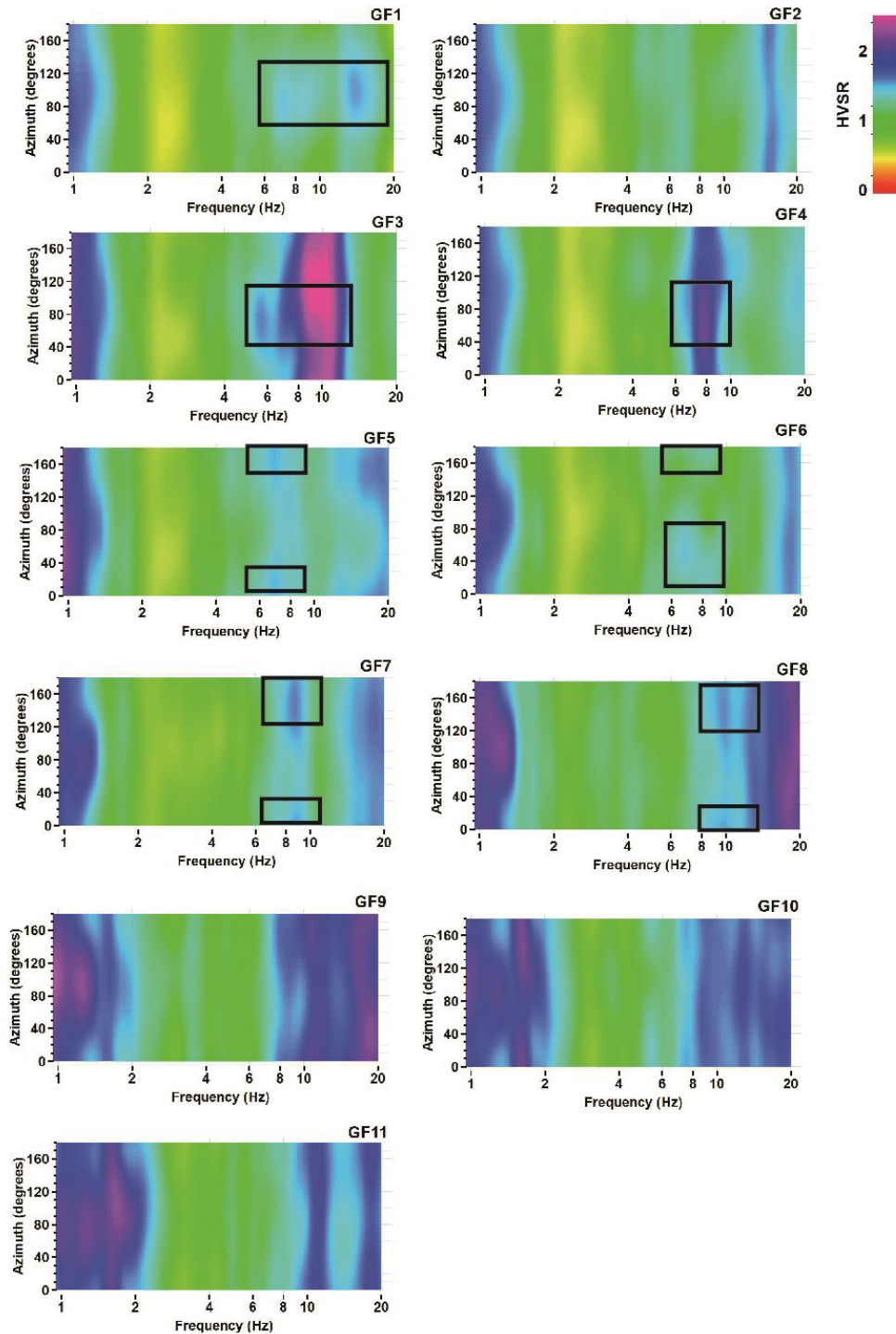
329

330

Fig. 7. Groups of HVSR curves.

331 Wavefield polarisation analysis was also applied to the ambient noise measurements (Fig. 8). The GF1, GF3, and GF4
332 stations show a slight polarisation with an azimuth of N80-100° for frequencies >6 Hz; the GF7 and GF8 records have a
333 similar characteristic, but with a slightly lower azimuth (N0-20°). The GF5 and GF6 stations seem to show a
334 transitional behaviour. The peaks in the range 0.2-1 Hz show a N120° polarisation in almost all the measurements (see
335 Supplementary Figure 1). This analysis may reveal the possible presence of high angle to sub-vertical structural or
336 paleo-morphological discontinuities within the sedimentary complex as they may tend to align the waves' oscillation
337 plane perpendicular to or at a high angle to the direction of the lineaments themselves.

338



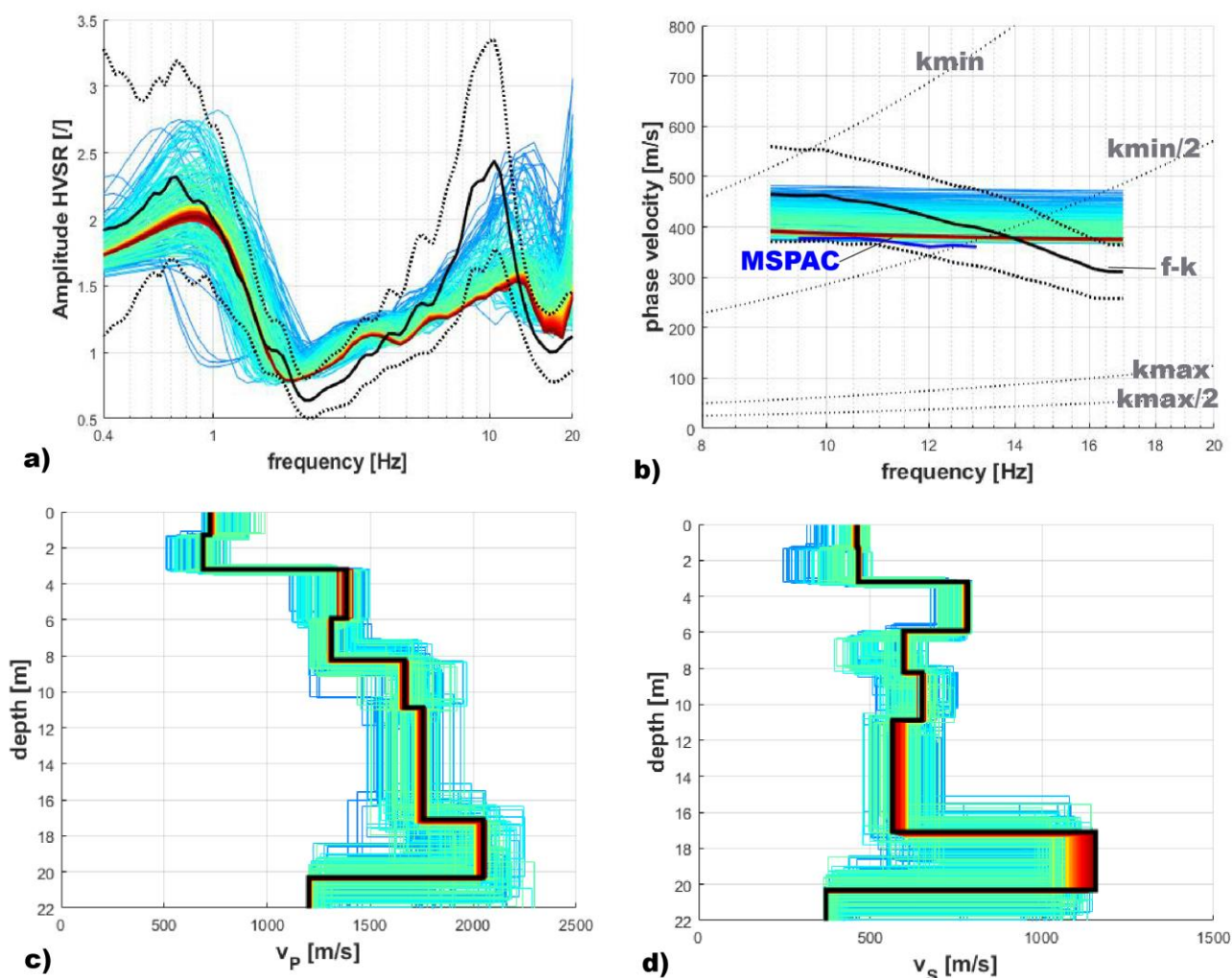
339

340 **Fig. 8.** Rotational HVSR results for each station, referring to the band 1-20 Hz for the clarity: HVSR curves plotted in
 341 the range 0.2-20 Hz may be found in the Supplementary Materials. Black boxes indicate the main polarisations:
 342 measurement at GF1 and GF3 sites show a slightly polarisation with an azimuth of N80-100° for frequencies >6 Hz,
 343 measurements at GF5 and GF6 sites show amplification in the band N0-20° and about N160-180°; measurement at GF7
 344 and GF8 sites show amplification in the band N0-20° and in a wider azimuthal range (about N120-180°).
 345

346 Regarding the 2D array measurement, since one of the hypotheses at the base of this method is the assumption of an
 347 infinite semi-space with parallel layers, before computing the dispersion curve, a control was made on the single spectra
 348 of the vertical component acquired at each geophone. This analysis led to the exclusion of eight geophones (four at each

349 extreme of the L-shaped array). The variability of the vertical components on all the geophones of the array is shown in
350 the Supplementary Figure 2.

351 The results from the 2D array are shown in Figure 9. These latter, as well as the frequencies highlighted by the HVS
352 curves, are useful for making inferences about the site's characterisation. Regarding the agreement shown in Fig. 9b, we
353 have overlapped the peaked f-k and MSPAC dispersion curves. Results showed that the combination of different
354 methods (f-k and MSPAC techniques) give complementary results. Average dispersion curves are comparable in the
355 range 9-13 Hz for both the techniques, and this increases the confidence about the results, while peaking the f-k
356 dispersion curve out of the bounds of the results obtained from MSPAC, remaining into the k_{max} and k_{min} limits,
357 allows extending the imaging towards highest frequencies. The general trend of the MSPAC curve seems similar to the
358 best-fit, while this latter is within the average and \pm standard deviation f-k dispersion curves.



359

360 **Fig. 9.** Results from 2D array measurement. The theoretical models of the fundamental mode Rayleigh-wave, in terms
361 of ellipticity curves and dispersion, are shown in (a) and (b), respectively. The colour scale is proportional to the misfit
362 resulting from the inversion, and the black curves are the measured dispersion and HVS curves. The phase velocities
363 in panel b are retrieved by the application of two methods (f-k and MSPAC) used for the processing of the 2D array
364 recording. v_P and v_S models are shown in (c) and (d), respectively.
365

366 **4.3. Soil-gas profiles**

367 Soil-gas concentrations (CO₂ and ²²²Rn) were measured along two profiles parallel to the ERT acquisitions, to verify the
 368 presence of possible structural or buried morphological discontinuities (faults, fractures, buried scarps) which provide
 369 routes for deep-gas leakages in correspondence to the low resistivity areas recognised in the ERT profiles. The data are
 370 reported in Table 1; the soil-gas samples exhibited concentrations of up to 10.6% for CO₂ and up to 7.98 kBq/m³ for
 371 ²²²Rn.

372 Along profile 1 (Fig. 10a), the spatial distribution of CO₂ and ²²²Rn values shows two peaks that occur between 100 and
 373 150 m, in correspondence with the low resistivity zone observed along ERT-1

374 Along profile 2 (Fig. 11a), the highest ²²²Rn activity (7.98 kBq/m³) was measured at the southern end of the profile, in
 375 correspondence with the high resistivity zone observed in the ERT-2 profile; CO₂ concentrations follow a trend similar
 376 to radon isotopes, but their values are relatively lower (up to 3.6%) than those measured along profile 1.

377

Distance from borehole m	CO ₂	²²² Rn
	%. v/v	kBq/m ³
<i>Profile 1</i>		
2	3.6	5.79
20	3.2	4.40
40	2.2	5.24
80	1.4	5.36
90	1.0	3.61
100	0.8	1.04
110	4.0	6.97
120	1.0	2.46
130	3.2	3.28
140	10.6	6.84
150	1.6	4.67
160	3.6	5.54
180	1.6	5.55
220	0.6	1.47
260	0.6	1.53
<i>Profile 2</i>		
9	3.6	5.79
18	1.0	3.14
27	2.8	6.68
36	3.0	7.98

378 **Table 1.** Soil-gas data collected along two profiles (location in Fig. 3).

379

380 **5. INTERPRETATION OF DATA AND DISCUSSION**

381 The correlation between borehole stratigraphy, geomorphological observations, geophysical, and geochemical data
 382 provides clues about the surface and subsurface geometry of the Prima Porta travertine body and the embedding

383 sediments which are useful for better defining the stratigraphic and morpho-structural architecture of this sector of the
384 Tiber valley.

385 In plan-view, the Prima Porta meander is featured by the lateral stack of several, east-directed, and convex-shaped scroll
386 bars (Fig. 12), which suggests a generalised eastward expansion of the entire meander point-bar and river-channel
387 system. Indeed, scroll bars typically record the incremental growth of a point-bar (Russell et al., 2018, with references);
388 in this case, they have been identified on map and on Google Earth images by small topographic irregularities (i.e.,
389 ridges and swales), by alignments of localised creeks, and by alternating belts of different soil moisture and vegetation
390 cover densities.

391 Regarding the subsoil structure, since the ERT-1 survey was performed in correspondence with the Prima Porta
392 borehole, it was possible to calibrate the ERT results and to directly correlate resistivity values with the litho-
393 stratigraphic characteristics. From top to bottom, the borehole, whose stratigraphy is shown in Figure 2b, intercepts
394 alluvial sediments (silt and clay of floodplain environment) attributed to the most recent phase of deposition of
395 overbank floods from the Tiber (middle-late Holocene, ~6 ka), which display a low resistivity (below 15 ohm×m); the
396 travertine layer, at depths between 9 and 12 m, and with an intermediate resistivity (Zone 2, green to yellow in Figs. 4
397 and 10c) between 15 and 30 ohm×m; beneath the travertine unit, the resistivity decreases again below 15 ohm×m, and
398 this zone matches the alluvial sediments (silt and silty sands) attributed to the lower portion of the buried terrace (Upper
399 Pleistocene) and to the underlying Paleotiber unit (Middle Pleistocene) in the core stratigraphy. These measures were
400 fundamental for attributing characteristic resistivities to the local deposits, which, in comparison with values from the
401 literature for the same sediments are generally low, especially those of the travertine (Pola et al., 2014; Huerta et al.,
402 2016; Török et al., 2019). This behaviour can be attributed to the quantity and quality of groundwater that almost
403 reaches the field level and is particularly mineralised (the electrical conductivity of water is 3080 $\mu\text{S}/\text{cm}$; Giustini et al.,
404 2018), generally reducing the resistivity (Loke and Barker, 1996; Loke and Dahlin, 2002; Oudeika et al., 2020).
405 At depths greater than 20 m, at a distance between 70 and 130 m from the origin of the profile, a zone with resistivity
406 values higher than 30 ohm×m (Zone 3), showing a sharp lateral variation of resistivity, is observed. There are no
407 borehole data that could aid in directly constraining the interpretation of this zone; however, considering the
408 stratigraphic architecture of the Tiber valley, this zone could be related both to gravels and sands from the basal channel
409 of the Paleotiber unit and/or to an even lower-occurring travertine body. The HVSR curves agree with both
410 interpretations. In fact, the GF1 to GF7 sites (Fig. 10b) show an inversion of S-wave velocities in the soil profile (i.e.,
411 with the presence of layers with a lower velocity with respect to the upper ones) which is consistent with lithoid
412 materials such as travertine and/or well-cemented gravels.

413 In the middle part of ERT-1, a wide zone of low resistivity values (<15 ohm×m) may be ascribed to saturated deposits
414 (probably silty and sandy alluvial sediments, based on the stratigraphic correlation; Giustini et al., 2020), characterised
415 by a remarkable presence of mineralised waters. Corresponding to this part of the section, the soil-gas profile shows two
416 peaks of CO₂ and ²²²Rn concentrations (Fig. 10a). Overall, low resistivity values and soil-gas anomalies suggest the
417 presence of a zone of intense water-fluid circulation, possibly associated with the presence of a structural or buried
418 morphological discontinuity (perhaps represented by the sharp lateral variation between Zones 2 and 3 of the ERT)
419 which allows the ascent of thermal waters and/or gas emissions. A CO₂-rich gas phase of deep origin (metamorphic
420 and partly mantle/magma degassing) is associated with the Prima Porta borehole, and several gas vents, locally
421 connected with crustal structural lineaments, have been documented along the Tiber valley (Vaselli et al., 1997;
422 Minissale et al., 2002; Giustini et al., 2018). Generally, deep-gas leakage is facilitated by faults and fractures because
423 they are deep, weakened zones consisting of highly fractured materials that increase permeability at the surface. The
424 migration of CO₂ and ²²²Rn by diffusion and/or advection along buried active faults can generate shallow anomalies
425 with concentrations significantly higher than background levels. Radon, a radioactive inert gas with a half-life of 3.82
426 days, is particularly sensitive to buried discontinuities because of its ability to migrate along relatively long distances
427 from host rocks, using CO₂ as a carrier gas (King et al., 1996; Ciotoli et al., 2007, 2014, 2016).

428 A fractures system in this part of the section could be also supported by the wavefield polarisation analysis. At
429 frequencies >6 Hz, the GF5, GF6, GF7, and GF8 sites show a slight polarisation, with an azimuth of N0-20°; a slight
430 polarisation is observed for sites GF1, GF3, and GF4 with an azimuth of N80-100° (Fig. 8). Moreover, a further
431 preferential direction is enhanced from the rotational HVSR at GF5, Gf6, GF7 and GF8: the measurements at GF5 and
432 GF6 sites show amplification in the band about N160-180°, while the measurements at GF7 and GF8 sites show
433 amplification in a wider azimuthal range (about N120-180°). To discuss the rationale behind this evidence, it should be
434 underlined that buried fault zones may be very challenging to investigate due to the complex geological structures (i.e.,
435 S-wave velocity inversion with depth) in which the combination of several phenomena of wave propagation (reflection,
436 resonance, Love wave trapping) modifies components with different weights and may render the interpretation difficult.

437 Nevertheless, many authors have demonstrated that, in fault zones, horizontal polarisation is often strong and tends to
438 be perpendicular to the fracture field or has a high-angle relative to the fault strike (Pischiutta et al. 2010, 2012, 2013,
439 2017; Napolitano et al., 2018 and reference therein; Panzera et al., 2016, 2017). The polarisation of the particle motion
440 of seismic noise is also known to be modified by heterogeneities in local structure such as cleavages or fractures (Ben
441 Zion, 1998; Pischiutta et al., 2012). Famiani et al. (2015) also identified peaks which were broader and with lower
442 amplitude and an important difference in terms of the signal polarisation across a seismogenic fault in central Italy (i.e.,
443 Pizzoli fault). Therefore, the observed polarisation in our data, further joined with the geochemical observations

444 discussed above, and the local fracture trends (N90-110°) traced in Figure 1, let us hypothesize a role of the fracture
445 systems (i.e., cracks) in the amplification at the study site.

446 In the eastern part of ERT-1, the resistivity Zone 2 overlies the high conductivity zone; it is located approximately at the
447 same level as the travertine deposit intercepted by the borehole. According to the resistivity values, this zone might be
448 interpreted on a first approximation as a large travertine body, extending between 150 m and the eastern end of the
449 ERT, slightly dipping towards the present-day Tiber river's course. However, the HVSR curves and soil-gas
450 concentrations do not bolster this interpretation. The HVSR curves, measured at the GF8, GF9 sites, show a very broad
451 band peak at higher frequencies (Figs. 5 and 7). Otherwise, the HVSR amplitude values in Fig. 10b at about 50 m from
452 the start of the W-E measurements alignment are lower than those measured in correspondence with the borehole; this
453 configuration is coherent with a relatively surficial horizon of materials with poor mechanical properties such as
454 relatively loose sands. This interpretation is confirmed by the low soil-gas concentrations measured with respect to the
455 other parts of the profile (Fig. 10a), typical of a very ventilated soil. Therefore, this resistivity zone can be interpreted as
456 being due to the lateral stack of sandy channel-fill bodies, consisting of eastward-migrating bars and featuring the
457 multilateral stacking pattern of channel bodies (Rajchl and Uličný, 2005; Gibling, 2006), which is a typical expression
458 of the channel clustering in the TDS' late transgressive and highstand systems tracts (Milli et al., 2016). The laterally
459 migrating bars in cross-sectional view correspond to the scroll bars on a plane shown in Figure 12. Relatively high
460 resistivity sand-dominated channel-fill bodies, which are embedded into more conductive floodplain fines, have
461 commonly been revealed by ERT investigations (Baines et al., 2002; Bersezio et al., 2007; Nimnate et al., 2017; Guinea
462 et al., 2018).

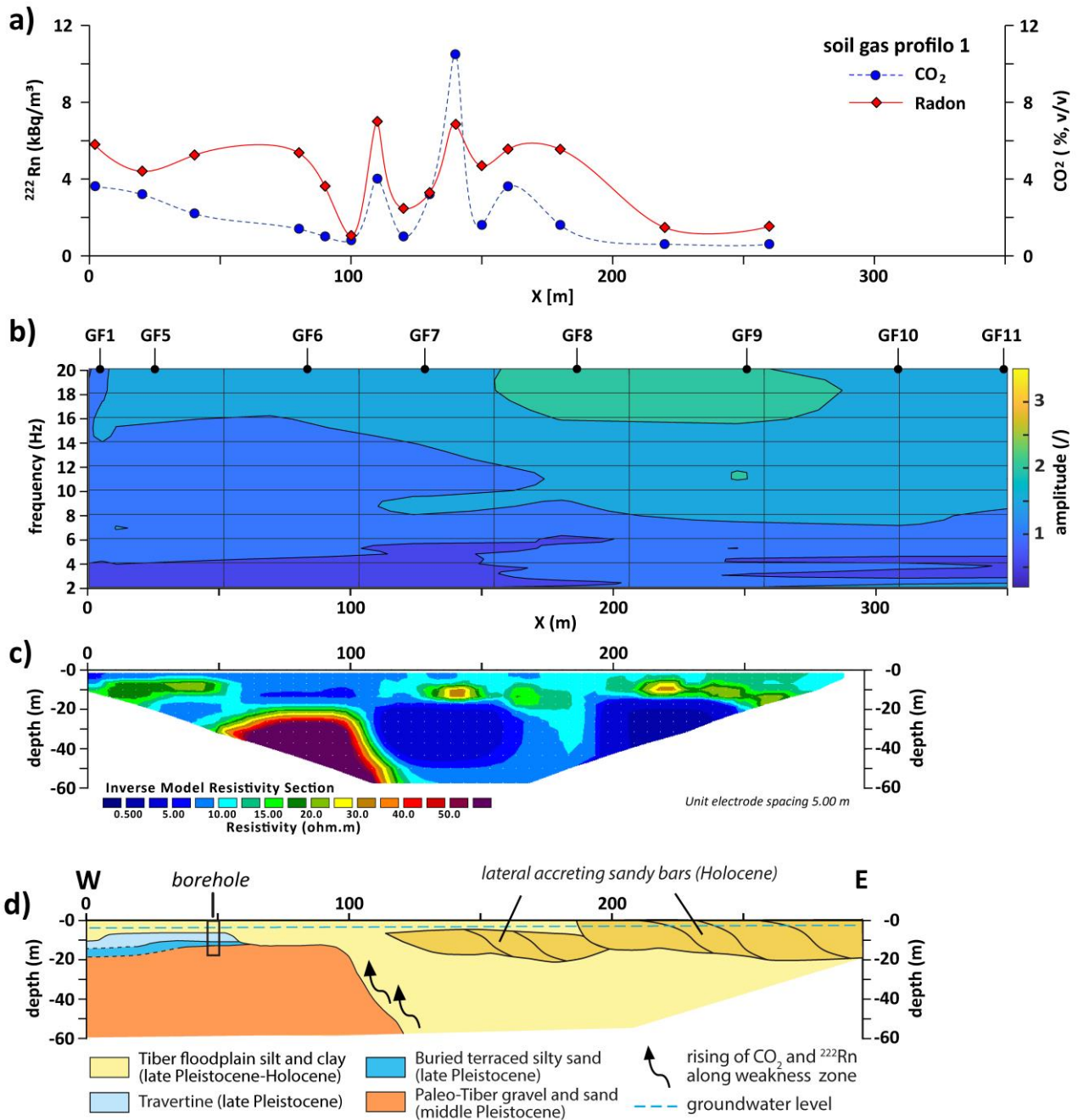
463 The two ERT arrays have a point of intersection between electrodes n. 7 (of the ERT-2) and n. 40 (of the ERT-1), and
464 ERT-2 also intercepts the travertine body, at a depth of about 4 m. In this tomography (Fig. 11c), travertine displays a
465 concave-upward section wedging out toward the central part of the profile; here, the resistivity tends to increase up to
466 50 ohm×m. A seismic refraction (SR) survey was performed above this high resistivity block; this measure allows one
467 to constrain the S-wave profile obtained throughout the 2D array measurement (Fig.11b) and to further confirm the
468 interpretation of this block as a unique travertine body. In fact, S-wave velocity increases up to 800 m/s in
469 correspondence with the high resistivity block, values that are compatible with compact and massive materials (Forte et
470 al., 2019). In contrast, the Zones 2 of resistivity, which are about 1.5 m thick and located just below surface in the
471 northern and southern parts of the profile, are not attributed to travertine, but to anthropogenic deposits – possibly a
472 buried basement of an old edifice whose perimeter is still recognisable in old satellite images. The other zones of lower
473 resistivity (<15 ohm×m) were interpreted as alluvial deposits covering the travertine.

474 Considering as a whole the high-strength structures of the two profiles, the upper surface of the travertine deposit
475 appears to have a curved shape, which is gently dipping towards the east (i.e., towards the present-day Tiber river), and
476 forms a concave-upward section wedging out toward the south; the maximum thickness could be 20 m. This curved
477 shape is consistent with the morphology inferred from macroscopic and microfacies observations (Giustini et al., 2020),
478 a pool in a terraced slope dam which is gently dipping towards the south and east. The real extension of the buried
479 travertine body is unknown, but we speculate that it is roughly extended along a N-S direction, along the western border
480 of the plain (Fig. 12), between the normal faults with roughly a NW-SE direction inferred from Funicello et al. (1992).
481 Ancient springs were probably connected to these structural features and related to the rising hydrothermal fluids
482 precipitating travertine.
483 The combined application of these ERT, seismic refraction, ambient noise measurements, and soil-gas survey
484 methodologies may be successfully used in similar geological contexts for identifying buried travertine bodies and other
485 complex 2D/3D structures. The alluvial valleys are often located in tectonically active areas, similarly to the Tiber
486 valley; travertine deposits can be quite common along their boundaries because they are associated with rising
487 hydrothermal fluids, whose ascent is favoured by the presence of structural discontinuities. In these contexts, travertine
488 deposits can potentially represent valuable archives of paleo-sources of CO₂ in places where gas emanations are no
489 longer visible, evidencing active tectonics and low-enthalpy geothermal areas.

490 1. CONCLUSIONS

491 The alluvial deposits of the Tiber river, at the Prima Porta site, were investigated using non-invasive geophysical and
492 geochemical methods. The results were calibrated and interpreted using previously collected litho-stratigraphic data of a
493 borehole drilled in the study area. The applied geophysical and geochemical techniques (ERT, seismic refraction,
494 ambient noise measurements, and CO₂ and ²²²Rn concentrations in soil-gas surveys) complement each other and their
495 combination allowed us to delineate the subsoil structure of this sector of the Tiber valley. In particular, the geometry of
496 the buried travertine body of Prima Porta was defined; its upper surface appears to have a curved shape, gently dipping
497 towards the east to the present-day Tiber river, and forming a concave-upward section wedging out toward the south.
498 Due to its hydrothermal origin, this travertine unit is a poorly porous, hard and crystalline material, and consequently its
499 specific electrical resistivity values were relatively high with respect to those measured in the embedding alluvial
500 sediments (silt and silty sands). This shape is consistent with the morphology inferred from macroscopic and
501 microfacies observations, i.e., a pool in a terraced slope dam (Giustini et al., 2020). Other stratigraphic and structural
502 features of this sector of the Tiber valley were inferred, such as the presence of silty-sand channels, deposited by the
503 Tiber river after the last glacial maximum. Finally, a weakness zone, permeable to the ascent of CO₂ and ²²²Rn, was

504 inferred in correspondence with low resistivity zone, a soil-gas anomaly, and slight polarisation effects recorded in the
 505 HVSR.
 506

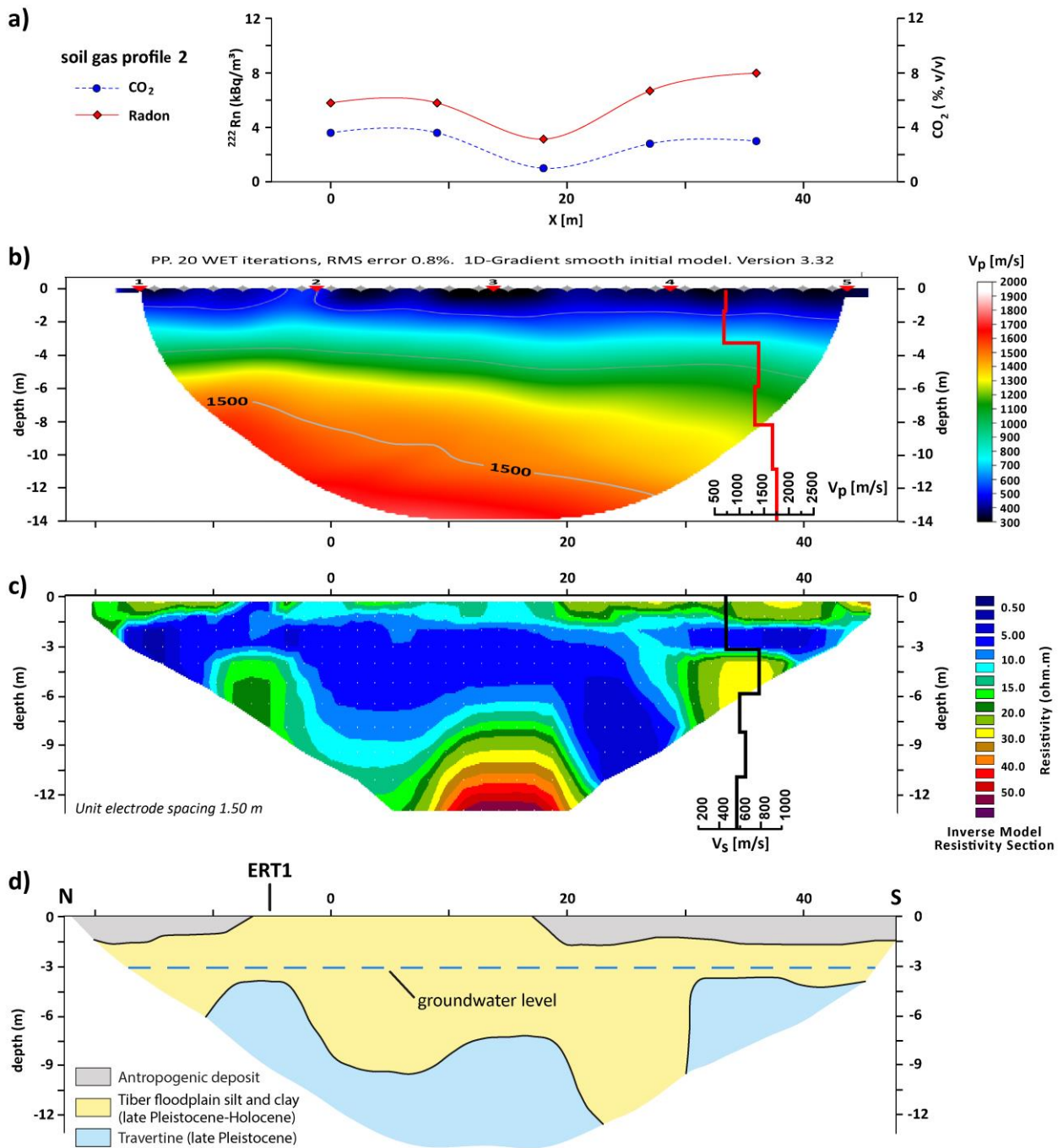


507

508

509 **Fig. 10.** a) Soil-gas (CO₂ and radon) profiles; b) HVSR cross-section; c) ERT-1; d) geological interpretation of the
 510 ERT-1 profile.
 511

512



513

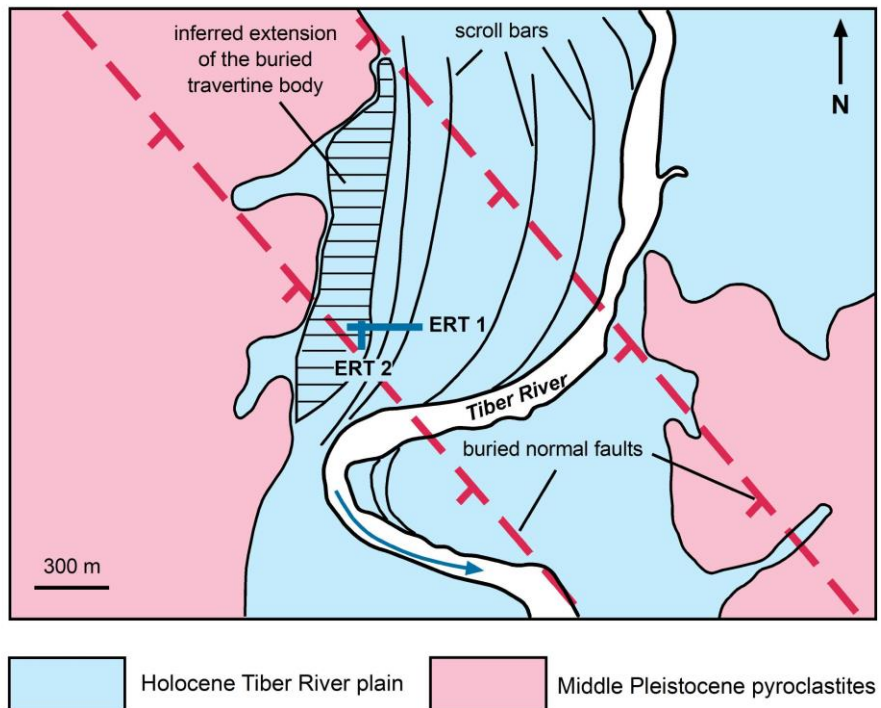
514

515

516

517

Fig. 11. a) Soil-gas (CO₂ and radon) profiles; b) V_p profile from the 2D array superimposed on SR section; c) V_s profile from the 2D array superimposed on ERT-2; d) geological interpretation of the ERT-2 profile.



518

519 **Fig. 12.** Sketch map showing the eastward-directed and convex-shaped scroll bars and the supposed extension of the
 520 buried travertine body. The buried inferred normal faults are from Funicello et al. (1992).

521

522 **ACKNOWLEDGEMENTS**

523 The authors are grateful to Gian Paolo Cavinato (IGAG-CNR) for his constructive comments and continue
 524 encouragement, and for providing software facilities for graphical elaborations. Prof. Giuseppe Della Monica and
 525 Francesco Basile (DST –Roma 3) are thanked for providing geophysical instruments for the ERT measurements and
 526 seismic refraction survey, and for the help during the geophysical survey, respectively. We also sincerely thank Azienda
 527 Agricola Orti del Canottiere, Giuseppe Capelli and Livio Manzetti for permitting the access to the study area. This
 528 study was partly funded by DTA.AD003.316 "Sistemi terrazzati" Project, Resp. Marco Mancini. The authors sincerely
 529 thank Jozef Müller, Andreas Goepel and the topic editor Thomas Voigt for their constructive comments and
 530 suggestions.

531

532 **CONFLICT OF INTEREST**

533 None of the material reported in the work has been published or is under consideration for publication elsewhere.
 534 Authors have no conflict of interest with any of the material presented.

535

536 **REFERENCES**

- 537 Asokhai, M.B., Egbai, J.C., Okolie, E.C., 2008. Using shallow reflection seismology for mapping bedrocks. *Nigerian*
538 *Journal of Science and Environment* 7, 66-72.
- 539 Ayolabi, E.A., Adeoti, L., Oshinlaja, N.A., Adeosun, I.O., Idowu, O.I., 2009. Seismic refraction and resistivity studies
540 of part of Igbogbo township, south-west Nigeria. *Journal of Scientific Research and Development* 11, 42-61.
- 541 Baines, D., Smith, D.G., Froese, D.G., Bauman, P., Nimeck, G., 2002. Electrical resistivity ground imaging (ERGI): a
542 new tool for mapping the lithology and geometry of channel-belts and valley-fills. *Sedimentology* 49, 441-449.
- 543 Barberi F., Buonasorte G., Cioni R., Fiordelisi A., Foresi L., Iaccarino S., Laurenzi M.A., Sbrana A., Vernia A., Villa
544 I.M., 1994. Plio–Pleistocene geological evolution of the geothermal area of Tuscany and Latium. *Memorie*
545 *descrittive della Carta Geologica d'Italia* 49, 77–135.
- 546 Beaubien, S.E., Jones, D.G., Gal, F., Barkwith, A.K.A.P., Braibant, G., Baubron, J.-C., Ciotoli, G., Graziani, S., Lister,
547 T.R., Lombardi, S., Michel, K., Quattrocchi, F., Strutt, M.H., 2013. Monitoring of near-surface gas geochemistry at
548 the Weyburn, Canada, CO₂-EOR site, 2001–2011. *International Journal of Greenhouse Gas Control* 16, S236-
549 S262, 10.1016/j.ijggc.2013.01.013
- 550 Ben-Zion, Y., 1998. Properties of seismic fault zone waves and their utility for imaging low-velocity structures. *Journal*
551 *of Geophysical Research Solid Earth* 103(B6), 12567-12585.
- 552 Bersezio, R., Giudici, M., Mele, M., 2007. Combining sedimentological and geophysical data for high-resolution 3-D
553 mapping of fluvial architectural elements in the Quaternary Po plain (Italy). *Sedimentary Geology* 202, 239-248.
- 554 Bettig, B., Bard, P.Y., Scherbaum, F., Riepl, J., Cotton, F., Cornou, C., Hatzfeld, D., 2005. Analysis of dense array
555 noise measurements using the modified spatial auto-correlation method (SPAC): application to the Grenoble area.
556 *Bollettino di Geofisica Teorica e Applicata* 42, 281-304.
- 557 Bridge J.S., 2003. *Rivers and floodplains: forms, processes and sedimentary record*. Blackwell, Oxford, pp. 491.
- 558 Carlucci, G., 2017. *Ambient noise data Analysis for the reconstruction of the deep subsurface model in the roman area*.
559 PhD thesis, University of Roma 3, Italy.
- 560 Castellaro, S., Mulargia, F., 2009. The effect of velocity inversions on H/V. *Pure and Applied Geophysics* 166(4), 567-
561 592.
- 562 Chiemeke, C.C., Aboh, H.O., 2012. Delineation of aquiferous layers within the basement complex using joint inversion
563 of seismic refraction tomography and high resolution 3D seismic reflection survey. *Archives of Applied Science*
564 *Research* 4, 400-405.
- 565 De Rita, D., Funicello, R., Corda, L., Sposato, A., Rossi, U., 1993. Volcanic Units. In: Di Filippo, M. (Ed.) *Sabatini*
566 *Volcanic Complex*. Quaderni della Ricerca Scientifica, C.N.R., Roma, 114, 33–79.
- 567 Ciotoli, G., Lombardi, S., Annunziatellis, A., 2007. Geostatistical analysis of soil gas data in a high seismic
568 intermontane basin: Fucino Plain, central Italy. *Journal of Geophysical Research* 112, B05407,
569 10.1029/2005JB004044.
- 570 Ciotoli, G., Bigi, S., Tartarello, C., Sacco, P., Lombardi, S., Ascione, A., et al., 2014. Soil gas distribution in the main
571 coseismic surface rupture zone of the 1980, Ms = 6.9, Irpinia earthquake (southern Italy). *Journal of Geophysical*
572 *Research Solid Earth* 119, 2440–2461. doi:10.1002/2013JB010508
- 573 Ciotoli, G., Etiope, G., Marra, F., Florindo, F., Giraudi, C., Ruggiero, L., 2016. Tiber delta CO₂-CH₄ degassing: a
574 possible hybrid, tectonically active Sediment-Hosted Geothermal System near Rome. *Journal of Geophysical*
575 *Research Solid Earth* 121, 48–69. doi:10.1002/2015JB012557
- 576 Cosentino, D., Cipollari, P., Marsili, P., Scrocca, D., 2010. Geology of the central Apennines: a regional review. In:
577 Beltrando, M., Peccerillo, A., Mattei, M., Conticelli, S., Doglioni, C., (Eds.) *The Geology of Italy: tectonics and life*
578 *along plate margins*. Journal of the Virtual Explorer, Electronic Edition, 36(12), doi: 10.3809/jvirtex.2010.00223.
- 579 De Filippis, L., Anzalone, E., Billi, A., Faccenna, C., Poncia, P.P., Sella P., 2013. The origin and growth of a recently-
580 active fissure ridge travertine over a seismic fault, Tivoli, Italy. *Geomorphology* 195, 13–26.

- 581 Di Bella, L., Carboni, M.G., Bergamin, L., 2002. Pliocene-Pleistocene foraminiferal assemblages of the middle and
582 lower Tiber Valley: stratigraphy and paleoecology. *Geologica Romana* 36, 129–145.
- 583 Faccenna, C., 1994 Structural and hydrogeological features of Pleistocene shear zones in the area of Rome (Central
584 Italy). *Annali di Geofisica* 37, 121-133.
- 585 Faccenna, C., Funiciello, R., 1993. Tettonica pleistocenica tra il Monte Soratte e i Monti Cornicolani. *Il Quaternario* 6,
586 103–118.
- 587 Famiani, D., Amoroso, S., Boncio, P., Bordoni, P., Cantore, L., Cara, F., Di Giulio, G., Di Naccio, D., Hailemichael, S.,
588 Mercuri, A., Milana, G., Vassallo, M., 2015. Noise measurements along fault zones in central Appenines. In: 6th Int
589 INQUA Meeting on Paleoseismology, Active Tectonics and Archaeoseismology, 19–24 April 2015, Pescara,
590 Fucino Basin, Italy. INGV, 146–149.
- 591 Forte, G., Chioccarelli, E., De Falco, M., Cito, P., Santo, A., Iervolino, I., 2019. Seismic soil classification of Italy
592 based on surface geology and shear-wave velocity measurements. *Soil Dynamics and Earthquake Engineering* 122,
593 79-93.
- 594 Foti, S., Hollender, F., Garofalo, F., Albarello, D., Asten, M., Bard, P-Y., Comina, C., Cornou, C., Cox, B., Di Giulio,
595 G., Forbriger, T., Hayashi, K., Lunedei, E., Martin, A., Mercerat, D., Ohrnberger, M., Poggi, V., Renalier, F.,
596 Sicilia, D., Socco, V., 2018. Guidelines for the good practice of surface wave analysis: a product of the
597 InterPACIFIC project". *Bulletin of Earthquake Engineering* 16, 2367–2420.
- 598 Funiciello, R., Parotto, M., 1978. Il substrato sedimentario nell'area dei Colli Albani: considerazioni geodinamiche e
599 paleogeografiche sul margine tirrenico dell'Appennino centrale. *Geologica Romana* 17, 233-287.
- 600 Funiciello, R., Giuliani, R., Marra, F., Salvi, S., 1992. Superfici strutturali plio-quadernarie al margine sud-orientale del
601 Distretto Vulcanico Sabatino. *Studi Geologici Camerti* spec. vol. 1991/2, CROP 11, 301–304.
- 602 Funiciello, R., Giuliani, R., Marra, F., Salvi, S., 1994. The influence of volcanism and tectonics on Plio–Quaternary
603 regional landforms in the Southeastern Sabatinian area (Central Italy). *Memorie descrittive della Carta Geologica
604 d'Italia* 49, 323–332.
- 605 Funiciello, R., Giordano, G., 2008. *Note illustrative della Carta Geologica d'Italia alla scala 1:50.000, Foglio 347
606 ROMA*. APAT–Servizio Geologico d'Italia, Roma
- 607 Funiciello, R., Giordano, G., 2010. *The Colli Albani Volcano*. International Association of Volcanology and Chemistry
608 of the Earth's Interior Special Publication 3, 400 pp.
- 609 Gabr, A., Murad, A., Baker, H., Bloushi K., Arman, H., Mahmoud, S., 2012. The use of seismic refraction and electrical
610 techniques to investigate groundwater aquifer, Wadi Al-ain, United Arab Emirates (UAE). In: Proceedings of the
611 International Conference on Water Resources and Wetlands Sept. 14-16, Tulcea-Romania, 94-99.
- 612 García-Jerez, A., Luzón, F., Sánchez-Sesma, F. J., Lunedei, E., Albarello, D., Santoyo, M. A., Almendros, J., 2013.
613 Diffuse elastic wavefield within a simple crustal model. Some consequences for low and high frequencies. *Journal
614 of Geophysical Research* 118(10), 5577–5595. doi:10.1002/2013JB010107
- 615 García-Jerez, A., Piña-Flores, J., Sánchez-Sesma, F.J., Luzón, F., Perton, M., 2016. A computer code for forward
616 calculation and inversion of the H/V spectral ratio under the diffuse field assumption. *Computers & Geosciences*
617 97, 67–78. doi:10.1016/j.cageo.2016.06.016
- 618 Gibling, M. R., 2006. Width and thickness of fluvial channel bodies and valley fills in the geological record: a literature
619 compilation and classification. *Journal of Sedimentary Research* 76, 731-770.
- 620 Giustini, F., Brilli, M., Mancini, M., 2018. Geochemical study of travertines along middle-lower Tiber valley (central
621 Italy): genesis, palaeo-environmental and tectonic implications. *International Journal of Earth Sciences* 107, 1321–
622 1342.
- 623 Giustini, F., Brilli, M., Di Salvo, C., Mancini, M., Voltaggio, M., 2020. Multidisciplinary characterization of the buried
624 travertine body of Prima Porta (Central Italy). *Quaternary International* 568, 65-78.

- 625 Guinea, A., Hollins, S., Meredith, K., Hankin, S., Cendón, D.I., 2018. Characterization of the subsurface architecture
626 and identification of potential groundwater paths in a clay-rich floodplain using multi-electrode resistivity imaging.
627 *Hydrological Sciences Journal* 63, 909-925.
- 628 Hinkle, M. E. (1994). Environmental conditions affecting concentrations of He, CO₂, O₂ and N₂ in soil gases. *Applied*
629 *Geochemistry* 9(1), 53-63.
- 630 Huerta, P., Armenteros, I., Tomé, O. M., González, P. R., Silva, P. G., González-Aguilera, D., Carrasco-García, P.,
631 2016. 3-D modelling of a fossil tufa outcrop. The example of La Peña del Manto (Soria, Spain). *Sedimentary*
632 *Geology* 333, 130–146.
- 633 Igboekwe, M.U., Ohaegbuchi, H.E., 2011. Investigation into the weathering layer using up-hole method of seismic
634 refraction. *Journal of Geology and Mining Research* 3, 73-86.
- 635 Kilner, M., West, L.J., Murray, T., 2005. Characterisation of glacial sediments using geophysical methods for
636 groundwater source protection. *Journal of Applied Geophysics* 57, 293-305. doi: 10.1016/j.jappgeo.2005.02.002
- 637 King, C. Y., King, B. S., Evans W. C., Zang W., 1996. Spatial radon anomalies on active faults in California. *Applied*
638 *Geochemistry* 11, 497–510.
- 639 Klusman, R.W., 1993. *Soil Gas and Related Methods for Natural Resource Exploration*. Wiley, England, pp. 483.
- 640 Konno, K., Ohmachi, T., 1998. Ground-motion characteristics estimated from spectral ratio between horizontal and
641 vertical components of microtremors. *Bulletin of the Seismological Society of America* 88, 228-241.
- 642 Lacoss, R., Kelly, T. E. J., Toksöz, M. N., 1969. Estimation of seismic noise structure using arrays. *Geophysics* 34(1),
643 21-38.
- 644 Loke, M.H., Barker, R.D., 1996. Practical technique for 3D resistivity surveys and data inversion. *Geophysical*
645 *Prospecting* 44, 499-523.
- 646 Loke, M.H., Dahlin, T., 2002. A comparison of Gauss-Newton and quasi-Newton methods in resistivity imaging
647 inversion. *Journal of Applied Geophysics* 49,149-162.
- 648 Lunedei, E., Malischewsky, P., 2015. A review and some new issues on the theory of the H/V technique for ambient
649 vibrations. In: Ansal, A., (Ed.), *Perspectives on European Earthquake Engineering and Seismology*, Springer,
650 Berlin, 371-394. https://doi.org/10.1007/978-3-319-16964-4_15
- 651 Malinverno, A., Ryan, W.B.F., 1986. Extension of the Tyrrhenian Sea and shortening in the Apennines as result of arc
652 migration driven by sinking lithosphere. *Tectonics* 5, 227-245.
- 653 Mancini, M., Cavinato, G.P., 2005. The Middle Valley of the Tiber River, central Italy: Plio-Pleistocene fluvial and
654 coastal sedimentation, extensional tectonics and volcanism. In: Blum, M.D., Marriott, S.B., Leclair, S.F. (Eds.),
655 *Fluvial sedimentology*. IAS Special Publication, vol. 35, Blackwell, Oxford, pp. 373–396.
- 656 Mancini, M., D'Anastasio, E., Barbieri, M., De Martini, P. M., 2007. Geomorphological, paleontological and 87Sr/86Sr
657 isotope analyses of early Pleistocene paleoshorelines to define the uplift of Central Apennines (Italy). *Quaternary*
658 *Research* 67(3), 487–501.
- 659 Marcucci, S., Milana, G., Hailemikaël, S., Carlucci, G., Cara, F., Di Giulio, G., Vassallo, M., 2019. The deep bedrock in
660 Rome, Italy: a new constraint based on passive seismic data analysis. *Pure and Applied Geophysics* 176(6), 2395-
661 2410.
- 662 Martinson, D.G., Pisias, N.G., Hayes, J.D., Imbrie, J., Moore, T.C. and Shackleton, N.J., 1987. Age dating and the
663 orbital theory of the ice ages development of a highresolution 0 to 300,000 year chronostratigraphy. *Quaternary*
664 *Research* 27, 1–29.
- 665 Miall A.D., 2014. *Fluvial Depositional Systems*. Springer, Cham, pp. 316.
- 666 Milli, S., Mancini, M., Moscatelli, M., Stigliano, F., Marini, M., Cavinato, G.P., 2016. From river to shelf, anatomy of a
667 high-frequency depositional sequence: the late Pleistocene to Holocene Tiber depositional sequence. *Sedimentology*
668 63, 1886–1928.

- 669 Minissale, A., Kerrick, D.M., Magro, G., Murrell, M.T., Paladini, M., Rihs, S., Sturchio, N.C., Tassi, F., Vaselli, O.,
670 2002. Geochemistry of Quaternary travertines in the region north of Rome (Italy): structural, hydrologic and
671 paleoclimatic implications. *Earth and Planetary Science Letters* 203, 709–728.
- 672 Nakamura, Y., 1989. A method for dynamic characteristics estimation of subsurface using microtremor on the ground
673 surface. *Quarterly Report of Railway Technical Research Institute* 30, 25–33.
- 674 Napolitano, F., Gervasi, A., La Rocca, M., Guerra, I., Scarpa, R., 2018. Site Effects in the Pollino Region from the
675 HVSR and Polarization of Seismic Noise and Earthquakes Site Effects in the Pollino Region from the HVSR and
676 Polarization of Seismic Noise and Earthquakes. *Bulletin of the Seismological Society of America* 108(1), 309-321.
- 677 Nimnate, P., Thitimakorn, T., Choowong, M., Hisada, K., 2017. Imaging and locating paleo-channels using geophysical
678 data from meandering system of the Mun River, Khorat Plateau, Northeastern Thailand. *Open Geosciences* 9, 675-
679 688.
- 680 Okiongbo, K.S., Akpofure E., Odubo, E., 2011. Determination of aquifer protective capacity and corrosivity of near
681 surface materials in Yenagoa city, Nigeria. *Research Journal of Applied Sciences, Engineering and Technology* 3,
682 785-791.
- 683 Oudeika, M.S., İlkimen, E.M., Taşdelen, S., Aydın A., 2020. Distinguishing Groundwater Flow Paths in Fractured Rock
684 Aquifers Formed Under Tectonic Stress Using Geophysical Techniques: Cankurtaran Basin, Denizli, Turkey.
685 *International Journal of Environmental Research* 14, 567–581.
- 686 Panzera, F., Lombardo, G., Monaco, C., 2016. New evidence of wavefield polarization on fault zone in the lower NE
687 slope of Mt. Etna. *Italian Journal of Geosciences* 135(2), 250-260.
- 688 Panzera, F., Lombardo G., Longo E., Langer H., Branca S., Azzaro R., Cicala V., Trimarchi F., 2017. Exploratory
689 seismic site response surveys in a complex geologic area: A case study from Mt. Etna volcano (southern Italy).
690 *Natural Hazards* 86(2), 385–399.
- 691 Patacca, E., Sartori, R., Scandone, P., 1990. Tyrrhenian basin and Apenninic arcs: Kinematics relations since Late
692 Tortonian times. *Memorie della Società Geologica Italiana* 45, 425–451.
- 693 Piña-Flores, J., Pertou, M., García-Jerez, A., Carmona, E., Luzón, F., Molina-Villegas, J.C., Sánchez-Sesma, F.J., 2017.
694 The inversion of spectral ratio H/V in a layered system using the diffuse field assumption (DFA). *Geophysical*
695 *Journal International* 208, 577-588.
- 696 Pischiutta, M., 2010. *The polarization of horizontal ground motion: an analysis of possible causes*. Ph.D. thesis,
697 Università di Bologna ‘Alma Mater Studiorum’, Italy.
- 698 Pischiutta, M., Salvini, F., Fletcher, J., Rovelli, A., Ben-Zion, Y., 2012. Horizontal polarization of ground motion in the
699 Hayward fault zone at Fremont, California: dominant fault-high-angle polarization and fault-induced cracks.
700 *Geophysical Journal International* 188(3), 1255-1272.
- 701 Pischiutta, M., Anselmi, M., Cianfarra, P., Rovelli, A., Salvini, F., 2013. Directional site effects in a non-volcanic gas
702 emission area (Mefite d’Ansanto, southern Italy): Evidence of a local transfer fault transversal to large NW–SE
703 extensional faults? *Physics and Chemistry of the Earth Parts A/B/C*, 63, 116-123.
- 704 Pischiutta, M., Fondriest, M., Demurtas, M., Magnoni, F., Di Toro, G., Rovelli, A., 2017. Structural control on the
705 directional amplification of seismic noise (Campo Imperatore, central Italy). *Earth and Planetary Science Letters*
706 471, 10-18.
- 707 Pola, M., Gandin A., Tuccimei P., Soligo M., Deiana R., Fabbri P., Zampieri D., 2014. A multidisciplinary approach to
708 understanding carbonate deposition under tectonically controlled hydrothermal circulation: a case study from a
709 recent travertine mound in the Euganean Hydrothermal System, northern Italy. *Sedimentology* 61, 172–199.
- 710 Qarqori, K., Rouai, M., Moreau, F., Saracco, G., Dauteuil, O., Hermitte, D., Boualoul, M., Le Carlier de Veslud, C.,
711 2012. Geoelectrical Tomography Investigating and Modeling of Fractures Network around Bittit Spring (Middle
712 Atlas, Morocco). *International Journal of Geophysics* 2012, 489634, <https://doi.org/10.1155/2012/489634>
- 713 Rajchl, M., Uličný, D., 2005. Depositional record of an avulsive fluvial system controlled by peat compaction
714 (Neogene, Most Basin, Czech Republic). *Sedimentology* 52, 601-625.

- 715 Russell, C.E., Mountney, N.P., Hodgson, D.M., Colombera, L., 2018. A novel approach for prediction of lithological
716 heterogeneity in fluvial point-bar deposits from analysis of meander morphology and scroll-bar pattern. In:
717 Ghinassi, M., Colombera, L., Mountney, N.P., Reesnik, A.J.H. (Eds.) *Fluvial Meanders and Their Sedimentary*
718 *Products in the Rock Record*. Int. Assoc. Sedimentol. Spec. Publ., 48, 385-418.
- 719 Sánchez-Sesma, F.J., Rodríguez, M., Iturrarán-Viveros, U., Luzón, F., Campillo, M., Margerin, L., García-Jerez, A.,
720 Suarez, M., Santoyo, M.A., Rodríguez-Castellanos, A., 2011. A theory for microtremor H/V spectral ratio:
721 application for a layered medium. *Geophysical Journal International* 186, 221–225. doi:10.1111/j.1365-
722 246X.2011.05064.x
- 723 Sánchez-Sesma, F.J., 2017. Modeling and inversion of the microtremor H/V spectral ratio: physical basis behind the
724 diffuse field approach. *Earth, Planets and Space* 6992. <https://doi.org/10.1186/s40623-017-0667-6>, 2017
- 725 Schumm, S.A., 1993. River response to base level change: implications for sequence stratigraphy. *Journal of Geology*
726 101, 279–294.
- 727 Sottili, G., Palladino, D. M., Zanon, V., 2004. Plinian activity during the early eruptive history of the Sabatini Volcani
728 District, Central Italy. *Journal of Volcanology and Geothermal Research* 135, 361–379.
- 729 Tentori, D., Marsaglia, K.M., Milli, S., 2016. Sand compositional changes as a support for sequence-stratigraphic
730 interpretation: the Middle Upper Pleistocene to Holocene deposits of the Roman Basins (Rome, Italy). *Journal of*
731 *Sedimentary Research* 86, 1208-1227.
- 732 Török, Á., Claes, H., Brogi, A., Liotta, D., Tóth, Á., Mindszenty, A., Kudó, I., Kele, S., Huntington, K.W., Shen C.-C.,
733 Swennen, R., 2019. A multi-methodological approach to reconstruct the configuration of a travertine fissure ridge
734 system: The case of the Cukor quarry (Süttő, Gerecse Hills, Hungary). *Geomorphology* 345, 106836.
- 735 Varughese, A., Kumar, P., Kumar, N., 2011. Seismic refraction survey a reliable tool for subsurface characterisation for
736 hydropower projects. *Proceedings of Indian Geotechnical Conference*, Dec. 15-17, Kochi, 137–139.
- 737 Vaselli, O., Tassi, F., Minissale, A., Capaccioni, B., Magro, G., Evans, W.C., 1997. Geochemistry of natural gas
738 manifestations from the Upper Tiber Valley (Central Italy). *Mineralogica et Petrographica Acta* 40, 201–212.
- 739 Ventriglia, U., 2002. *Geologia del territorio del Comune di Roma*. Provincia di Roma. Rome, pp. 810.
- 740 Wathelet, M., Chatelain, J. L., Cornou, C., Giulio, G. D., Guillier, B., Ohrnberger, M., & Savvaidis, A., 2020. Geopsy:
741 A user-friendly open-source tool set for ambient vibration processing. *Seismological Research Letters* 91(3), 1878–
742 1889.